Computational Geosciences (2019) 23:849–880
https://doi.org/10.1007/s10596-019-9818-0

ORIGINAL PAPER

Direct simulation of pore-scale two-phase visco-capillary flow on large digital rock images using a phase-field lattice Boltzmann method on general-purpose graphics processing units

F. O. Alpak[1,2] · **I. Zacharoudiou**[3] · **S. Berg**[4,5,6] · **J. Dietderich**[1] · **N. Saxena**[1]

Received: 14 May 2018 / Accepted: 31 March 2019 / Published online: 22 July 2019
© Springer Nature Switzerland AG 2019

Abstract

We describe the underlying mathematics, validation, and applications of a novel Helmholtz free-energy—minimizing phase-field model solved within the framework of the lattice Boltzmann method (LBM) for efficiently simulating two-phase pore-scale flow directly on large 3D images of real rocks obtained from micro-computed tomography (micro-CT) scanning. The code implementation of the technique, coined as the eLBM (energy-based LBM), is performed in CUDA programming language to take maximum advantage of accelerated computing by use of multinode general-purpose graphics processing units (GPGPUs). eLBM's momentum-balance solver is based on the multiple-relaxation-time (MRT) model. The Boltzmann equation is discretized in space, velocity (momentum), and time coordinates using a 3D 19-velocity grid (D3Q19 scheme), which provides the best compromise between accuracy and computational efficiency. The benefits of the MRT model over the conventional single-relaxation-time Bhatnagar-Gross-Krook (BGK) model are (I) enhanced numerical stability, (II) independent bulk and shear viscosities, and (III) viscosity-independent, nonslip boundary conditions. The drawback of the MRT model is that it is slightly more computationally demanding compared to the BGK model. This minor hurdle is easily overcome through a GPGPU implementation of the MRT model for eLBM. eLBM is, to our knowledge, the first industrial grade–distributed parallel implementation of an energy-based LBM taking advantage of multiple GPGPU nodes. The Cahn-Hilliard equation that governs the order-parameter distribution is fully integrated into the LBM framework that accelerates the pore-scale simulation on real systems significantly. While individual components of the eLBM simulator can be separately found in various references, our novel contributions are (1) integrating all computational and high-performance computing components together into a unified implementation and (2) providing comprehensive and definitive quantitative validation results with eLBM in terms of robustness and accuracy for a variety of flow domains including various types of real rock images. We successfully validate and apply the eLBM on several transient two-phase flow problems of gradually increasing complexity. Investigated problems include the following: (1) snap-off in constricted capillary tubes; (2) Haines jumps on a micromodel (during drainage), Ketton limestone image, and Fontainebleau and Castlegate sandstone images (during drainage and subsequent imbibition); and (3) capillary desaturation simulations on a Berea sandstone image including a comparison of numerically computed residual non-wetting-phase saturations (as a function of the capillary number) to data reported in the literature. Extensive physical validation tests and applications on large 3D rock images demonstrate the reliability, robustness, and efficacy of the eLBM as a direct visco-capillary pore-scale two-phase flow simulator for digital rock physics workflows.

Keywords Free-energy lattice Boltzmann method · LBM · Phase-field method · Cahn-Hilliard equation · Navier-Stokes equations · Pore-scale flow simulation · Two-phase flow · Computational fluid dynamics · CFD · Multiple-relaxation-time · MRT · Digital rock physics · DRP · General-purpose graphics processing unit · GPGPU · Parallel computing · Snap-off · Haines jumps · Forced drainage · Forced imbibition · Residual oil

1 Introduction

Understanding the dynamics of immiscible displacement at the pore scale can provide beneficial insights into the pore-scale characteristics and flow regimes that have a major

✉ F. O. Alpak
Omer.Alpak@shell.com

Extended author information available on the last page of the article.

influence on the macroscale displacement process [68]. Moreover, pore-scale flow simulation can facilitate the computation of the Darcy-scale flow parameters necessary as input for, e.g., reservoir simulation. However, it is a very complicated study due to numerous factors influencing the flow such as fluid density and viscosity, interfacial tension, fluid flow rate, surface wettability, pore geometry, and medium heterogeneity [67]. Besides the experimental studies, our knowledge of immiscible displacement can be complemented by numerical modeling, where experimental studies in pore scale are high in cost and usually time consuming [68]. Also, in an experimental study of a special parameter's effect on flow behavior, it is troublesome to set other parameters constant when the special parameter changes. Although numerical simulation cannot consider all aspects of immiscible displacement in complex geometries arising in natural porous media, it can give a general overview of the fluid flow mechanism and can be a helpful predictive tool [21]. Ultimately, at our current state of knowledge, numerical simulation of multiphase flow, improved oil recovery (IOR), and enhanced oil recovery (EOR) processes is, in many cases, the only practical methodology to upscale flow and displacements from pore to Darcy scale. For that reason, numerical simulation approaches covering multiphase flow and IOR/EOR processes at pore-scale resolution have received increasing interest. These approaches group into two major families. The first are so-called pore network models [22] where the pore space is abstracted into a network of spherical pore bodies connected with tubes of polygonal cross sections, and flow and displacement are described mechanistically by rules. In order to avoid the associated approximations and shortcomings [19], direct numerical approaches, which are becoming increasingly feasible, are used. In direct numerical pore-scale flow simulation, hydrodynamic flow equations are solved directly on the complex pore space extracted, for instance, from X-ray micro-computed tomography.

Direct numerical simulation approaches are particularly appropriate for modeling pore-scale flow because no a priori choice between the level of rigor and captured phenomena is made. Moreover, simulations are performed directly on segmented images that describe the pore structure without introducing remeshing uncertainties. Unlike traditional pore network modeling techniques and morphological modeling approaches (e.g., the maximum inscribed sphere technique) [89], in direct simulation, capillary and viscous forces act at the same time. Thus, depending on the choice of flow parameters, both capillary- and viscous-dominated flows can be rigorously captured. Direct simulation enables the description of a wide range of flow regimes and simulation of a wide range of pore-scale dynamics such as cooperative and/or nonlocal displacement processes. Berg et al. [19] state that such nonlocal processes have been observed during drainage in 2D micromodels [8] and during imbibition [18] with fast micro-CT (e.g., [17]). However, from a computational perspective, direct simulation techniques are notably more computationally expensive than pore network models.

For single-phase flow, direct simulation techniques are more well established and, to some extent, commercially available in software packages. For two-phase flow, the underlying transport phenomena are substantially more complex, and active research is ongoing along various tracks. Several methods have been developed for simulating single- and two-phase flows at molecular, pore, and other meso scales. These methods include lattice gas and lattice Boltzmann models (e.g., [23]), Monte Carlo models (e.g., [64]), molecular dynamics (e.g., [86]), smoothed particle hydrodynamics (SPHs) (e.g., [90]), dissipative particle dynamics (DPD) (e.g., [66]), and Eulerian computational fluid dynamics (CFD). The latter family of techniques includes the front-tracking method (e.g., [42]), the volume of fluid method (e.g., [83]), the level-set method (e.g., [81]), and the phase-field method (e.g., [3, 4, 13, 34, 38, 52, 56]). Recently, Demianov et al. [30, 31] and Dinariev and Evseev [33] introduced the density functional hydrodynamics method within the framework of the finite-volume method, where the modeling of two-phase pore-scale flow has been demonstrated [9, 17] using a general formulation, which accounts for the miscibility effects [59]. The density functional hydrodynamics method is closely related to the phase-field method in terms of its thermodynamically based fundamentals. The Eulerian CFD family of techniques and the lattice Boltzmann technique are more commonly used for simulating fluid flow phenomena at the pore scale. We refer the reader to the reviews of pore-scale flow simulation methods by Anderson et al. [7], Jakobsen [53], Meakin and Tartakovsky [70], Joekar-Niasar et al. [54], Kim [57], and Blunt et al. [21]. The phase-field method, originally developed within the framework of the finite-volume/finite-element method, is closely related to the method described in this paper, which is developed within the framework of the lattice Boltzmann method (LBM).

LBM is recently proposed as an ideal CFD method for simulation of two-phase flow through complicated geometry of porous media. Unlike continuum CFD schemes which are based on discretization of macroscopic continuum equations, LBM is based on the mesoscopic kinetic equations (e.g., Benzi et al. [14] and Succi [91]). The fundamental advantage of LBM is its computational efficiency. The method was designed from ground up to run-on high-performance hardware to accommodate for complex physics. The ensuing efficiency makes new scientific frontiers accessible when it allows to solve problems that could not be approached before. Thus, LBM eliminates the computational inefficiencies resulting from solving differential equations with the brute-force approach of classical CFD. Algorithm simplicity and accuracy in handling irregular flow paths are the main reasons for LBM's rapid progress in multiphase flow modeling through porous media (e.g., [11, 12, 41]). It is also an explicit method that makes the code suitable to massively parallel computing [49]. There are four predominant multiphase LBM models in the literature which are as follows: (1) the R-K color gradient method (e.g., [44, 94]), (2) the Shan-Chen pseudo-potential model (e.g., [60, 88]), (3) the free-energy model [92], and (4) the mean-field theory model [46]. Huang et al. [49] have recently used the R-K color gradient method to simulate two-phase flow in a porous medium constructed by scattered circles with different radii. They conducted simulation in 17 cases with various viscosity ratios and capillary numbers to show flow pattern distributions in a logarithmic plot of viscosity ratio versus capillary number. Armstrong et al. [11, 12] used an R-K color gradient LBM on a mixed CPU-GPU supercomputer to simulate multiphase flow in a sandstone rock over a wide range of saturation and capillary numbers demonstrating also close agreement with direct imaging in terms of fluid topology. Dong et al. [35] utilized the Shan-Chen model to study the viscous fingering phenomenon of the displacement of two immiscible fluids in simplified homogeneous porous media. They tested the effects of capillary number, Bond number, viscosity ratio, and surface wettability on flow behavior. Liu and Wu [68] applied the Shan-Chen model and volume of fluid (VOF) method to examine the effects of wettability, interfacial tension, and pressure gradient on two-phase flow in a very complex 3D model of a real porous medium. Liu et al. [67] extended the mean-field theory model to investigate the effects of capillary number, viscosity ratio, contact angle, and bond number on the immiscible displacement of gas and liquid in a 2D homogeneous pore network.

The R-K color gradient and Shan-Chen LBM models use a simplistic description of the fluid-fluid interface which captures only limited physics. While being sufficient and successful for two-phase immiscible situations [11, 12], it is difficult to extend the methodology in a thermodynamically consistent form for fluid systems with compositional gradients, varying interfacial properties, and immiscible-miscible transitions. The phase-field approach is very suitable to handle such situations [59]. There are also respective free-energy–based LBM models, which were originally proposed by Swift et al. [92, 93]. These models involve a thermodynamic equilibrium function of phases, and a defining term of interfacial tension is added to the equilibrium distribution function, allowing the free-energy model to define the interfacial tension more easily than the other multiphase models. During recent years, several developments have been performed on this model, e.g., by Pooley and Furtado [78] and Inamuro et al. [51], and in a major advance, Zheng et al. [102] developed a computationally inexpensive model which is applicable at high viscosity ratios and recovers the lattice Boltzmann equation to the Cahn-Hilliard equation [27] without any additional terms.

Yang [96] performed a quantitative comparison of the Shan-Chen pseudo-potential model, the R-K color gradient model, and an implementation of the free-energy model. It has been found that the Shan-Chen model allows the simulation of high-density ratio fluids (e.g., liquid-gas systems) but gives rise to low numerical stability and wide interfaces for multiphase immiscible systems (e.g., oil-water systems). On the other hand, the R-K color gradient model and the free-energy model readily permit the simulation of two-phase flow for fluids with significant viscosity contrast and recover the analytical solutions of Poiseuille flow and fingering simulations. Yang [96] concluded that the free-energy and R-K color gradient models are most appropriate to simulate immiscible two-phase pore-scale flow of fluids exhibiting high viscosity contrast with high numerical stability.

While the free-energy LBM is a thermodynamically based model where there is a direct link between interfacial curvatures and interfacial tension as an upscaled quantity (stemming from the actual nanoscale characteristics of the interface), the R-K color gradient model lacks such a direct link to the thermodynamics, which renders it unsuitable for subsurface applications in hydrocarbon recovery. Therefore, we focus on the free-energy model for the LBM implementation. We describe the development, validation, and application of a distributed parallel implementation of a variant of the free-energy LBM based on the phase-field method for simulating two-phase pore-scale flow in a thermodynamically consistent fashion on large images of porous rocks. The numerical method solves the hydrodynamic visco-capillary equations of motion for a binary fluid with viscosity contrast. The continuity and Navier-Stokes equations are coupled to an advection-diffusion equation and are solved using a free-energy lattice Boltzmann algorithm. The key element of the method is a free-energy functional that describes the equilibrium properties of the binary fluid. Construction, advancement, destruction, and regeneration of phase interfaces are governed by this free-energy functional. The pressure tensor and the chemical potential are both derived from this functional. As such, they provide a gateway for the thermodynamically based free-energy minimization concept to enter into pore-scale two-phase flow equations. We implement a multiple-relaxation-time (MRT) lattice Boltzmann algorithm that reduces the spurious velocities at the fluid-fluid interface near the contact line [78] and leads to an improvement in numerical stability. The code implementation of this algorithm is coined as the energy-based lattice Boltzmann method (eLBM), standing for energy-based lattice Boltzmann method. While individual components of eLBM can be separately identified in various references, our novel contributions are (1) integrating all computational and high-performance computing components together into a unified industrial grade simulator implementation and (2) providing extensive and definitive quantitative validation results with eLBM in terms of robustness and accuracy for a variety of flow domains including a plethora of real rock images. Novel predictions of fluid topology and relative permeability during imbibition by the use of eLBM have already been published in Alpak et al. [1]. To our knowledge, this paper is unique in the open literature in terms of completeness in model description and eLBM code implementation detail, as well as comprehensiveness in terms of fundamental validation tests on real rock images.

The outline of this paper is as follows: We first describe the mathematical model on which the machinery of the eLBM code is based. The following section elaborates on the algorithmic parameters of eLBM. Subsequently, a set of smaller-scale validation problems is presented which establishes that eLBM contains the right level of physical rigor for the applications at interest. Contrary to pore network models where Darcy-scale results are obtained by a combination of displacement rules and extensive tuning of the network, direct simulation approaches rely entirely on the correctness of the elementary pore-scale displacement mechanisms. The purpose of the small-scale validation tests is to establish that phenomena associated with the elementary displacement physics are handled by the simulator in a correct way. A series of basic validation tests has been established in the literature [9, 100] which probes the interplay of viscous and capillary forces. The geometry-constrained snap-off was chosen as the first physical validation problem as it involves topological changes of fluid interfaces [9]. Simulation-based studies of Haines jumps constitute the next detailed study using both a synthetically generated micromodel and a micro-CT image volume of a Ketton limestone, a Fontainebleau sandstone, and a Castlegate sandstone. For the latter cases, the possibility of correctly modeling Haines jumps using a thermodynamically consistent two-phase pore-scale simulation method is demonstrated for both forced-drainage and forced-imbibition processes. The studies of Haines jumps on the Ketton limestone, Fontainebleau sandstone, and Castlegate sandstone images involve large-scale flow simulations from the computational perspective. A section on the summary of the work and conclusions closes this document.

2 Mathematical model and implementation

2.1 Thermodynamics of the fluid

There is a direct link between interfacial curvatures and interfacial tension as an upscaled quantity in free-energy LBM. This is a major requirement for a model intended for a pore-scale multiphase IOR/EOR flow simulator. Thus, we implement the free-energy LBM at the core of our pore-scale flow simulator.

The free-energy LBM is a variant of the phase-field method that belongs to a class of hydrodynamic models called the diffuse interface models where the fluid-fluid interface has a finite thickness [7]. Earlier versions of the free-energy LBM are described in Swift et al. [92, 93], Briant et al. [25], and Briant and Yeomans [24]. Far away from a contact line, the free-energy LBM solves the hydrodynamic equations of motion of the fluid, i.e., the Navier-Stokes equations and the continuity equation. In the vicinity of the contact line, however, due to the finite thickness of the interface, the method introduces a diffusive mechanism, which regularizes the viscous dissipation singularity [29] and allows the contact line to slip on a solid substrate. One of the most important advantages of the method is that, when simulating a binary fluid, this approach avoids the need to track the time evolution of the interface between two different phases [97]. This makes it ideal to study problems involving the time evolution of driven fluid-fluid interfaces, such as the ones that emerge in pore-scale two-phase displacement processes. The two phases contain particles of two different types in the standard binary model that is used in this work. The two phases have the same density but may have different viscosities. The free-energy model is known to deliver enhanced stability for problems with large viscosity ratios between displacing and displaced fluids. The free-energy model can also describe (partially) miscible binary systems [3].

Let Ω denote a spatial domain such that $\Omega \subset R^3$ and let $J := \left(0, t_f\right)$ denote the considered time interval with end (final) time, $t_f \in R^+$. We use the index (also known as Einstein) notation throughout the paper for expressing the summations in partial differential equations. The symbols α, β, and γ denote the component summation indices. The equilibrium properties of a binary (two-phase) fluid can be described by a Helmholtz free-energy functional [24]

$$F = \int_V \left(f_b + \frac{\kappa_\phi}{2} \left(\partial_\alpha \phi\right)^2 \right) dV + \int_S f_s dS, \tag{1}$$

where the first term is a volume (V) integral over the spatial domain (fluids) and the second term is a surface (S) integral over the surfaces of the spatial domain (solid-fluid interfaces). The first term in the integrand is the bulk free-energy density given by

$$f_b = \frac{A}{2}\phi^2 + \frac{B}{4}\phi^4 + \frac{c^2}{3}\rho\ln\rho, \tag{2}$$

where ϕ is the order parameter, ρ is the fluid mass density, and c is a lattice velocity parameter. The order parameter is defined as $(m_1 - m_2)\big/(m_1 + m_2)$, where m_1 and m_2 are mass densities of Phase 1 and Phase 2 fluid, respectively. This choice of f_b allows binary phase separation into two phases if $A<$ and $B>$, as the bulk free-energy density takes the form of a double-well potential, with bulk equilibrium solutions $\phi_{eq} = \pm\sqrt{(-A\,/B)}$. Here, we make the choice $A = -B$, which leads to $\phi_{eq} = \pm 1$ for the two phases. The position of the interface is chosen to be at $\phi = 0$. The final term in the bulk free-energy density, $\frac{c^2}{3}\rho ln\rho$, does not affect the phase behavior and is added to enforce incompressibility [55].

The gradient term $\frac{\kappa_\phi}{2}(\partial_\alpha\phi)^2$ in Eq. 1 penalizes the spatial variations of the order parameter ϕ, for example across an interface, and ensures a smooth transition from one phase to the other; hence, this term is related to the interfacial tension $\sigma = \sqrt{8\kappa_\phi A}\,/9$ and to the interface width $\xi = \sqrt{-\kappa_\phi}\,/A$ [24].

The final term in the free-energy functional (Eq. 1) describes the interactions between the fluid and the solid surfaces. Following Cahn [26], the surface energy density is taken to be of the form $f_s = -h\phi_s$, where ϕ_s is the value of the order parameter at the surface. Minimization of the free-energy gives an equilibrium wetting boundary condition [24]

$$\kappa_\phi\partial_\perp\phi = -\frac{df_s}{d\phi_s} = -h, \tag{3}$$

which permits the computation of the value of the normal derivative of the order parameter $\partial_\perp\phi$ at the substrate in equilibrium. The value of the parameter h (surface excess chemical potential) is related to the equilibrium contact angle θ^{eq} via [24]

$$h = \sqrt{2\kappa_\phi(-A)}\,sign\left[\frac{\pi}{2} - \theta^{eq}\right]\sqrt{cos\left(\frac{\alpha}{3}\right)\left[1 - cos\left(\frac{\alpha}{3}\right)\right]}, \tag{4}$$

where $\alpha = arccos\left(sin^2\theta^{eq}\right)$ and the function $sign$ returns the sign of its argument.

This choice of the free-energy leads to the (exchange) chemical potential

$$\mu = \frac{\delta F}{\delta\phi} = A\phi - A\phi^3 - \kappa_\phi\partial_{\gamma\gamma}\phi, \tag{5}$$

which describes the change in F for a small change in the order parameter and is constant at equilibrium. The pressure tensor, which determines how the system approaches equilibrium, is given by Anderson et al. [7] and Kendon et al. [55]

$$\begin{aligned} P_{\alpha\beta} &= \left[\phi\frac{\delta F}{\delta\phi} + \rho\frac{\delta F}{\delta\rho} - F\right]\delta_{\alpha\beta} + (\partial_\alpha\phi)\frac{\delta F}{\delta(\partial_\beta\phi)} \\ &= \left[p_b - \kappa_\phi\phi\partial_{\gamma\gamma}\phi - \frac{\kappa_\phi}{2}(\partial_\gamma\phi)^2\right]\delta_{\alpha\beta} + \kappa_\phi(\partial_\alpha\phi)(\partial_\beta\phi) \\ &= P^{iso}\delta_{\alpha\beta} + P^{chem}_{\alpha\beta}, \end{aligned} \tag{6}$$

where $p_b = \frac{c^2}{3}\rho + \frac{1}{2}A\phi^2 - \frac{3}{4}A\phi^4$ is the bulk pressure. The pressure tensor comprises of two terms, a "chemical" pressure tensor contribution $\left(P^{chem}_{\alpha\beta}\right)$ and an isotropic contribution $\left(P^{iso}\right)$ to ensure constant density [55]. $P^{chem}_{\alpha\beta}$ originates from the fact that, in the presence of concentration (represented by the order-parameter) gradients, there is a thermodynamic force density $(-\phi(\partial_\alpha\mu))$ acting at each point of the fluid which can be expressed as the divergence of a chemical pressure tensor: $\phi(\partial_\alpha\mu) = \partial_\beta P^{chem}_{\alpha\beta}$. Effectively this thermodynamic force density pulls the two fluids in opposite directions due to the chemical potential gradient, with the net force being zero at the interface ($\phi = 0$). For a free-energy–based multicomponent LBM we refer the reader to Li and Wagner [65] and Zhang and Kwok [101].

2.2 Equations of motion

The hydrodynamic equations for the system are the continuity (Eq. 7) and the Navier-Stokes (Eq. 8) equations for a non-ideal fluid

$$\partial_t\rho + \partial_\alpha(\rho u_\alpha) = 0, \tag{7}$$

$$\partial_t(\rho u_\alpha) + \partial_\beta(\rho u_\alpha u_\beta) = -\partial_\beta P_{\alpha\beta} + \partial_\beta\left[\eta\left(\partial_\beta u_\alpha + \partial_\alpha u_\beta\right)\right] + F_\alpha, \tag{8}$$

where $\mathbf{u}$, $\mathbf{P}$, η, and $\mathbf{F} = \rho\mathbf{g}$ denote the fluid velocity, pressure tensor, dynamic viscosity, and body force, respectively. For a binary fluid, the equations of motion are coupled with an advection-diffusion equation

$$\partial_t\phi + \partial_\alpha(\phi u_\alpha) = M\nabla^2\mu, \tag{9}$$

which describes the dynamics of the order parameter ϕ. $M = M(\phi)$ denotes the mobility coefficient, which is nonlinear in ϕ and restricts the diffusion to the vicinity of fluid-fluid interfaces. Details of our nonlinear mobility implementation will be introduced in Section 2.3 of the paper. We refer the reader to Kim [57] on the use of constant versus variable mobility. We use the phase-weighted description of the velocity. The equilibrium thermodynamic properties of the fluid enter the equations of motion through the pressure tensor (Eq. 6) and the chemical potential (Eq. 5).

By expanding the chemical potential (μ) in powers of $\phi - \phi_{eq}$, one obtains the following expression for small deviations from equilibrium

$$\mu = \left(A - 3A\phi_{eq}^{2}\right)\left(\phi - \phi_{eq}\right) + O\left(\left(\phi - \phi_{eq}\right)^{2}\right), \tag{10}$$

The diffusive term $M\nabla^{2}\mu$ can be written as $D\nabla^{2}\phi$ with $D = M\left(A - 3A\phi_{eq}^{2}\right)$ corresponding to the diffusion coefficient. Then, Eq. 9 can be expressed as follows:

$$\partial_{t}\phi + \partial_{\alpha}\left(\phi u_{\alpha}\right) = D\nabla^{2}\phi, \tag{11}$$

We target the isothermal immiscible flow of two flowing fluids within the application scope of the pore-scale simulator. We assume that the thermal effects due to fluid-fluid and fluid-rock friction are negligible. Therefore, the energy balance equation is consciously excluded in the equations of motion. Moreover, in the current eLBM implementation, we assume that the contact angle hysteresis [82], i.e., the differences between advancing and receding contact angles from the equilibrium contact angle, is negligible.

The equations of motion (Eq. 7 through Eq. 11) are solved using an MRT implementation of LBM [28]. Details about the implementation of this technique are given in the references Briant and Yeomans [24], Yeomans [97], and Pooley et al. [79]. The continuity and Navier-Stokes equations are coupled to an advection-diffusion equation and are not solved independently. This ensures that the equations are solved with an algorithm, which is consistent with the thermodynamics of the fluids. Thermodynamic concepts enter the equations of motion through the chemical potential and pressure tensor in this formulation. The coupling occurs at the level of the distribution functions for the density and in the pressure tensor. Details of this can be found in Briant and Yeomans [24], Yeomans [97], and Pooley et al. [79]. The evolution of the order parameter is obtained from solving the advection-diffusion equation. The order parameter responds to the flow as it can be advected by the flow (while velocity field is obtained from solving the Navier-Stokes and continuity equations), but it also responds to chemical potential gradients. The evolution of the order-parameter field results in a change of the pressure field, which, in turn, affects the flow field.

Due to the continuity equation (Eq. 7), we are free to specify only three of the four variables (density and the three components of the velocity) on the boundary. The fourth variable will be the outcome of solving the equations of motion using the lattice Boltzmann algorithm [47].

2.3 Phase-field LBM implementation for a binary fluid

From the viewpoint of representation of approximated solution variables on a discrete grid, LBM (including eLBM) is an Eulerian technique as it operates on a fixed mesh. However, there are Lagrangian and arbitrary Lagrangian-Eulerian implementations of LBM in the literature as well (e.g., [43, 71, 95]).

Real-life two-phase pore displacement scenarios have fluids with different densities. Having stated that, we restrict the scope of the pore-scale immiscible flow simulator to flows where the density contrast is relatively small, and the viscosity contrast is a more dominant factor over density contrast, e.g., displacement of oil with water or vice versa. We consciously exclude the density contrast–driven systems from the applicability scope of the simulator. On the other hand, this scope definition presents us with the opportunity to make the binary fluid assumption (i.e., density-matched fluids) in the simulator formulation and thereby takes advantage of the computational efficiency it endows the simulator with in terms of the LBM solver implementation.

Conventional methods directly solve the Navier-Stokes equations in terms of the density (ρ) and velocity (u) and approximate the differential equations by the use of a finite-difference, finite-volume or finite-element method. On the contrary, LBM introduces a number (Q) of particle distribution functions $f_{i}\left(\mathbf{r},t\right)$ $\left(i = 0, \cdots, Q-1\right)$, discrete in time and space, which are associated to a set of velocity directions (e_{i}). These distribution functions can be interpreted as the density of fluid, at position $\mathbf{r}$ and time t, which is moving in direction i. Figure 1 shows the directions

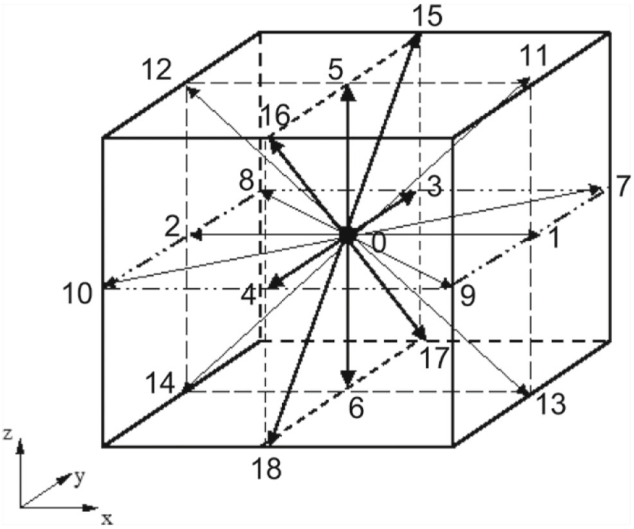

Fig. 1 The velocity vectors e_{i} in the 19-velocity, three-dimensional lattice Boltzmann model (D3Q19)

of the velocities in a 3D model with 19 velocity vectors (D3Q19) given by

$$\begin{bmatrix} e_{x,0-6} \\ e_{y,0-6} \\ e_{z,0-6} \end{bmatrix} = \begin{bmatrix} 0 & c & -c & 0 & 0 & 0 & 0 \\ 0 & 0 & 0 & c & -c & 0 & 0 \\ 0 & 0 & 0 & 0 & 0 & c & -c \end{bmatrix}, \tag{12a}$$

$$\begin{bmatrix} e_{x,7-18} \\ e_{y,7-18} \\ e_{z,7-18} \end{bmatrix} = \begin{bmatrix} c & -c & c & -c & 0 & 0 & 0 & 0 & c & -c & c & -c \\ c & c & -c & -c & c & -c & c & -c & 0 & 0 & 0 & 0 \\ 0 & 0 & 0 & 0 & c & c & -c & -c & c & c & -c & -c \end{bmatrix}, \tag{12b}$$

where $c{=}\Delta x \big/ \Delta t$ is the lattice velocity parameter and Δx and Δt are the discretization in space and time, respectively.

The moments of the velocity distribution functions (f_i) are related to the physical quantities, mass density (ρ), and momentum density ($\rho\mathbf{u}$) via

$$\sum\nolimits_{i=0}^{18} f_i{=}\rho, \quad \sum\nolimits_{i=0}^{18} f_i e_{i\alpha}{=}\rho v_\alpha, \tag{13}$$

where $\mathbf{v}$ is related to the fluid velocity ($\mathbf{u}$) through

$$\rho u_\alpha{=}\rho v_\alpha{+}\frac{1}{2}F_\alpha \Delta t. \tag{14}$$

The time evolution of the distribution functions (f_i) follows two steps:

$$\text{Collision step: } f_i^{'}(\mathbf{r},t){=}f_i(\mathbf{r},t){-}\frac{1}{\tau_f}\left[f_i(\mathbf{r},t){-}f_i^{eq}(\mathbf{r},t)\right]{+}\Delta t F_i, \tag{15a}$$

$$\text{Propagation step: } f_i(\mathbf{r}{+}\mathbf{e_i}\Delta t, t{+}\Delta t){=}f_i^{'}(\mathbf{r},t), \tag{15b}$$

where f_i^{eq}, τ_f, and F_i are the local equilibrium distribution functions, the relaxation time and the external body force acting on the fluid, respectively. Equation 15b represents one of the simplest collision models, proposed by Bhatnagar et al. [20], where a single-relaxation-time approximation is made. The distribution functions (f_i) relax towards their equilibrium values (f_i^{eq}) with a relaxation time (τ_f), which is related to the dynamic viscosity of the fluid by

$$\eta{=}\rho c^2 \Delta t\left(\tau_f{-}1\big/2\right)\big/3\ . \tag{16}$$

The relaxation time (τ_f) therefore has to be greater than $1\big/2$. The collision step is followed by a propagation step (Eq. 15b), where populations (f_i) stream to the next lattice site along e_i.

In order to recover the continuity equation (Eq. 7)) and the Navier-Stokes equation in the continuum limit, the following restrictions should be imposed on the distribution functions and on the forcing term:

$$\sum\nolimits_{i=0}^{18} f_i^{eq}{=}\rho, \quad \sum\nolimits_{i=0}^{18} f_i^{eq} e_{i\alpha}{=}\rho u_\alpha, \\ \sum\nolimits_{i=0}^{18} f_i^{eq} e_{i\alpha}e_{i\beta}{=}P_{\alpha\beta}{+}\rho u_\alpha u_\beta, \tag{17a}$$

$$\sum\nolimits_{i=0}^{18} f_i^{eq} e_{i\alpha}e_{i\beta}e_{i\gamma}{=}\frac{\rho c^2}{3}\left(u_\alpha\delta_{\beta\gamma}{+}u_\beta\delta_{\alpha\gamma}{+}u_\gamma\delta_{\alpha\beta}\right),$$

$$\sum\nolimits_{i=0}^{18} F_i{=}\rho, \quad \sum\nolimits_{i=0}^{18} F_i e_{i\alpha}{=}F_\alpha, \\ \sum\nolimits_{i=0}^{18} F_i e_{i\alpha}e_{i\beta}{=}u_\alpha F_\beta{+}u_\beta F_\alpha. \tag{17b}$$

For a binary fluid, two sets of particle distribution functions are needed, since there are two fluid phases: one of them (f_i) is related to the density and momentum (Eqs. 13 and 14) and the other (g_i) is related to the order parameter

$$\sum\nolimits_{i=0}^{18} g_i{=}\ \phi, \tag{18}$$

Again, the evolution of the additional distribution functions follows two steps:

$$\text{Collision step: } g_i^{'}(\mathbf{r},t){=}g_i(\mathbf{r},t){-}\frac{1}{\tau_g}\left[g_i(\mathbf{r},t){-}g_i^{eq}(\mathbf{r},t)\right], \tag{19a}$$

$$\text{Propagation step: } g_i(\mathbf{r}{+}\mathbf{e_i}\Delta t, t{+}\Delta t){=}g_i^{'}(\mathbf{r},t), \tag{19b}$$

where g_i^{eq} is the equilibrium distribution functions. The relaxation time (τ_g) is related to the mobility coefficient in the advection-diffusion equation (Eq. 9) by

$$M{=}\ \Delta t\Gamma\left(\tau_g{-}1\big/2\right)(\phi{-}1)(\phi{+}1), \tag{20}$$

where Γ is a parameter that governs the slip velocity of the contact line, as the contact line moves via diffusion. Γ can be predicted using a calibration procedure involving high-resolution visualizations of micromodel experiments for a given fluid-fluid-solid triplet with an equilibrium contact angle (θ^{eq}), approximately matching the actual simulation problem at hand. Moreover, if the simulation problem at hand warrants so and if there is a justifiable way of generating spatial variability, one can specify a heterogeneous Γ for a heterogeneous θ^{eq} problem.

The distribution functions $\left(g_i^{eq}\right)$ must obey the following constraints:

$$\sum\nolimits_{i=0}^{18} g_i^{eq}{=}\phi, \quad \sum\nolimits_{i=0}^{18} g_i^{eq} e_{i\alpha}{=}\phi u_\alpha, \\ \sum\nolimits_{i=0}^{18} g_i^{eq} e_{i\alpha}e_{i\beta}{=}\ \Gamma\mu\delta_{\alpha\beta}{+}\phi u_\alpha u_\beta \tag{21}$$

to correctly reproduce the advection-diffusion equation (Eq. 9).

Taking into account the constraints in Eqs. 17a and 21 for f_i^{eq}, g_i^{eq}, and F_i, the equilibrium distribution functions and the forcing terms can be defined as follows [78]:

$$f_i^{eq}=\frac{w_i}{c^2}\left(p_b-\kappa_\phi\nabla^2\phi+e_{i\alpha}\rho u_\alpha+\frac{3}{2c^2}\left[e_{i\alpha}e_{i\beta}-\frac{c^2}{3}\delta_{\alpha\beta}\right]\rho u_\alpha u_\beta\right),$$
$$\frac{\kappa_\phi}{c^2}\left(w_i^{xx}\partial_x\phi\partial_x\phi+w_i^{yy}\partial_y\phi\partial_y\phi+w_i^{zz}\partial_z\phi\partial_z\phi+w_i^{xy}\partial_x\phi\partial_y\phi\right.$$
$$\left.+w_i^{xz}\partial_x\phi\partial_z\phi+w_i^{yz}\partial_y\phi\partial_z\phi\right), \quad (22)$$

$$g_i^{eq}=\frac{w_i}{c^2}\left(\Gamma\mu+e_{i\alpha}\phi u_\alpha+\frac{3}{2c^2}\left[e_{i\alpha}e_{i\beta}-\frac{c^2}{3}\delta_{\alpha\beta}\right]\phi u_\alpha u_\beta\right), \quad (23)$$

and

$$F_i=\frac{w_i}{c^2}\left(e_{i\alpha}F_\alpha+\frac{3}{2c^2}\left[e_{i\alpha}e_{i\beta}-\frac{c^2}{3}\delta_{\alpha\beta}\right]\left(u_\alpha F_\beta+u_\beta F_\alpha\right)\right). \quad (24)$$

The coefficients w_i, w_i^{xx}, w_i^{yy}, w_i^{zz}, w_i^{xy}, w_i^{xz}, and w_i^{yz} are as follows:

$$w_{1-6}=\frac{1}{6}, \quad (25a)$$
$$w_{7-18}=\frac{1}{12}, \quad (25b)$$
$$w_{1,2}^{xx}=w_{3,4}^{yy}=w_{5,6}^{zz}=\frac{5}{12}, \quad (25c)$$
$$w_{3-6}^{xx}=w_{1,2,5,6}^{yy}=w_{1-4}^{zz}=-\frac{1}{3}, \quad (25d)$$
$$w_{7-10}^{xx}=w_{15-18}^{xx}=w_{7-14}^{yy}=w_{11-18}^{zz}-\frac{1}{24}, \quad (25e)$$
$$w_{11-14}^{xx}=w_{15-18}^{yy}=w_{7-10}^{zz}=\frac{1}{12}, \quad (25f)$$
$$w_{1-6}^{xy}=w_{1-6}^{yz}=w_{1-6}^{xz}=0, \quad (25g)$$
$$w_{7,10}^{xy}=w_{11,14}^{yz}=w_{15,18}^{xz}=\frac{1}{4}, \quad (25h)$$
$$w_{8,9}^{xy}=w_{12,13}^{yz}=w_{16,17}^{xz}=-\frac{1}{4}, \quad (25i)$$
$$w_{11-18}^{xy}=w_{7-10}^{yz}=w_{15-18}^{yz}=w_{7-14}^{xz}=0. \quad (25j)$$

Although the choice for the coefficients in Eqs. 22 through 24 is not unique, it was shown that this choice reduces the unphysical currents, called spurious velocities, that appear close to the curved interfaces in lattice Boltzmann simulations [78]. It is important to note that the distribution functions f_i^{eq} and g_i^{eq} are coupled to each other through the terms $\partial_\alpha\phi$ and $\nabla^2\phi$ in f_i^{eq}.

The hydrodynamic equations of motion, namely continuity equation (Eq. 7), Navier-Stokes equation (Eq. 8), and advection-diffusion equation (Eq. 9) can be obtained by performing a Chapman-Enskog expansion [69] on Eqs. 15a and 20.

Consistent with the physics of pore-scale two-phase flow of two immiscible fluids, e.g., oil and water, the variant of LBM implemented in the eLBM code approximates the incompressible Navier-Stokes equations for two-phase flow. The derivation of the incompressible Navier-Stokes equations by means of the LBM is only valid for low Mach numbers (typically, $Ma<0.1$) with $Ma=u_{0,l}\big/c_s$, where $u_{0,l}$ is the characteristic velocity in lattice units and c_s is the speed of sound, which is a lattice constant such that $c_s^2=1\big/3$. Theoretically, even at low Ma values, the Reynolds number $(Re=\rho u_{0,l}l\big/\eta)$ can be high due to a low viscosity (η), rendering LBM applicable for any Re. However, the viscosity is directly related to the relaxation time in practice. For stability reasons, the relaxation time is limited at the lower and upper bounds. Therefore, the practically accessible Re range is approximately 1.0×10^{-4} to 1.0.

The developments reported in this paper are a step towards a more comprehensive model including compositional and density gradient effects. In the future, we intend to relax the density-matched fluid assumption. In order to achieve this objective, the momentum balance equation needs to be extended for density contrast.

2.4 Initial and boundary conditions

The fluids are at rest in the flow domain (Ω) as the initial condition. The order parameter (ϕ) and bulk pressure (p_b) fields can be homogeneous (e.g., before primary drainage) or heterogeneous (e.g., post-drainage/pre-imbibition) within the pore space initially.

In lattice Boltzmann simulations, we encounter two main boundary conditions on solid surfaces: the no-slip boundary condition for the velocity field and the wetting boundary condition (Eq. 3) for the order parameter.

A no-slip boundary refers to the condition at a solid boundary, where the fluid has zero velocity relative to the boundary. The solid walls are introduced to the lattice Boltzmann model through the implementation of the midlink bounce-back method proposed by Ladd and Verberg [61], where the incoming populations ($f_i^{'}$) are reflected towards the lattice nodes they came from. In the 3D formulation, the advected populations ($f_i^{'}$), which are traveling along links connecting fluid and solid nodes, are reflected towards the fluid node they came from. This step can be described by $f_{-i}\left(\mathbf{r},t+\Delta t\right)=f_i^{'}\left(\mathbf{r},t\right)$, where the direction $-i$ denotes the opposite direction of the direction i. The bounce-back step is repeated at the end of each cycle of the collision-propagation sequence and ensures that the no-slip boundary condition is recovered at the solid boundaries. More precisely, the effective boundary, defined as the position of the zero-velocity plane, is located halfway between the fluid and solid nodes.

We next consider the implementation of the wetting boundary condition. The value of the normal derivative of the order parameter $\partial_\perp\phi$ at the substrate in equilibrium is expressed by Eq. 3. Using this condition and the values for ϕ at the fluid nodes neighboring the boundary, we assign the appropriate values for ϕ at the neighboring solid nodes. The main advantage of this method is that the terms $\partial_\alpha \phi$ and $\nabla^2 \phi$, needed for the evaluation of f_i^{eq} in Eq. 22, can be calculated in the same way as for the fluid nodes in the bulk. We use the stencils for $\partial_\alpha \phi$ and $\nabla^2 \phi$ reported in Pooley and Furtado [78] that were shown to reduce spurious velocities. Since eLBM is based on a phase-field method that results in diffuse interfaces and operates directly on image volumes stemming from imaging and image processing that often contain jagged surfaces (with artificial roughness due to insufficient resolution), it is prone to the errors associated with the inaccurate representation of the energy density on rough surfaces. We counter this prohibitive issue in eLBM by implementing the energy-based correction methodology described in Frank et al. [39] such that the wetting boundary condition is accurately imposed within two-phase flow simulations.

Prescribed velocity and prescribed order-parameter boundary conditions are implemented for the inlet to drive the fluid flow through the domain (Ω). Gradient-free fluid-exit boundary conditions are implemented for the outlet to mimic the real-life situation that the medium in which the flow takes place is much larger than the domain we numerically model. A loop boundary condition is imposed for the order parameter and velocity on the open-to-flow, i.e., non-solid global faces of the domain (Ω). The loop boundary condition is similar to the popular periodic boundary condition but does not require mirroring of the domain. A fluid package that exits the domain at a given domain boundary surface enters the domain at the opposing boundary surface with the same order parameter and velocity, as long as there is a fluid cell at the entry point.

2.5 MRT approximation

We implement a variant of the MRT method for computing the relaxation times in eLBM [2, 28, 55, 63, 80]. The rationale for that is as follows: When a single-relaxation-time approximation is used to model a binary fluid consisting of phases with different viscosities, strong spurious velocities appear at the fluid-fluid interface near the contact point [78]. This results in an incorrect equilibrium contact angle (θ_{eq}), since the system is continuously pushed out of equilibrium. Spurious currents originate from long-range contributions to the equilibrium distribution functions near the contact line and from the bounce-back boundary conditions. Making the choice $\tau_f = 1$ overcomes the problem. However, τ_f controls the fluid viscosity through Eq. 16 and hence, it is not possible to keep it to unity for both phases of a binary fluid if the two phases have different viscosities.

Pooley et al. [79] showed that introducing an MRT approximation [28, 80] significantly suppresses the spurious currents. This is achieved by eliminating the effect of the nonhydrodynamic modes by setting the relaxation time for these modes to $\tau_f = 1$, which results in automatically setting the distribution functions to their equilibrium values (f_i^{eq}) at each time step. A different relaxation time (τ_f) is used for the hydrodynamic modes, which accounts for the different viscosities of the two fluid phases. Moreover, an important remark is that the introduction of the MRT approach improves the numerical stability of the algorithm [55]. It is important to note that the MRT approximation is not required for g_i since the mobility coefficient M in Eq. 9 can be tuned by the independent parameter Γ through Eq. 20. This allows us to fix the relaxation time to $\tau_g = 1$ for g_i The use of the MRT technique for formulating the collision operator allows eLBM access more stable simulations for large viscosity ratios.

The main idea of the MRT method is that different relaxation times are used for different linearly independent combinations of the distribution functions (f_i). The relaxation parameters responsible for generating the viscous terms in the Navier-Stokes equations (Eq. 8) are set to τ_f, those related to conserved quantities to infinity, and all the others, which correspond to nonhydrodynamic modes, to unity.

In the evolution equation of the distribution functions (f_i) (Eq. 14), the collision term $\frac{1}{\tau_f}\left(f_i - f_i^{eq}\right)$ is replaced by

$$\mathbf{M}^{-1} \cdot \mathbf{S} \cdot \mathbf{M}\left[\mathbf{f} - \mathbf{f}^{eq}\right], \tag{26}$$

where f_i and f_i^{eq} are now written as column vectors $\mathbf{f}$ and $\mathbf{f}^{eq}$, respectively. The matrix $\mathbf{M}$ performs a change of basis, such that the new basis contains more physically relevant variables. We use the choice for $\mathbf{M}$ reported by Du et al. [36], which is a 19 × 19 matrix. For this choice, the first row will give the fluid density (ρ) when dotted with $\mathbf{f}$, while the fourth, sixth, and eighth rows will give the components of the momentum density: ρu_x, ρu_y, and ρu_z, respectively. The 10th, 12th, 14th, 15th, and 16th rows correspond to the components of the symmetric traceless viscous stress tensor: $3p_{xx}$, $p_{yy} - p_{zz}$, p_{xy}, p_{yz}, and p_{zz}, respectively. The remaining rows are related to other "kinetic" (nonhydrodynamic) moments [28, 80].

Each of the row vectors in $\mathbf{M}$ is mutually orthogonal, and therefore its inverse is given by

$$\mathbf{M}_{ij}^{-1} = \frac{1}{\sum_k \mathbf{M}_{jk}^2} \mathbf{M}_{ji}. \tag{27}$$

The matrix $\mathbf{S}$ in Eq. 26 is diagonal and given by

$$\mathbf{S} = diag\left(0, 1, 1, 0, 1, 0, 1, 0, 1, \varpi_f, 1, \varpi_f, \varpi_f, 1, \varpi_f, \varpi_f, \varpi_f, 1, 1, 1\right), \tag{28}$$

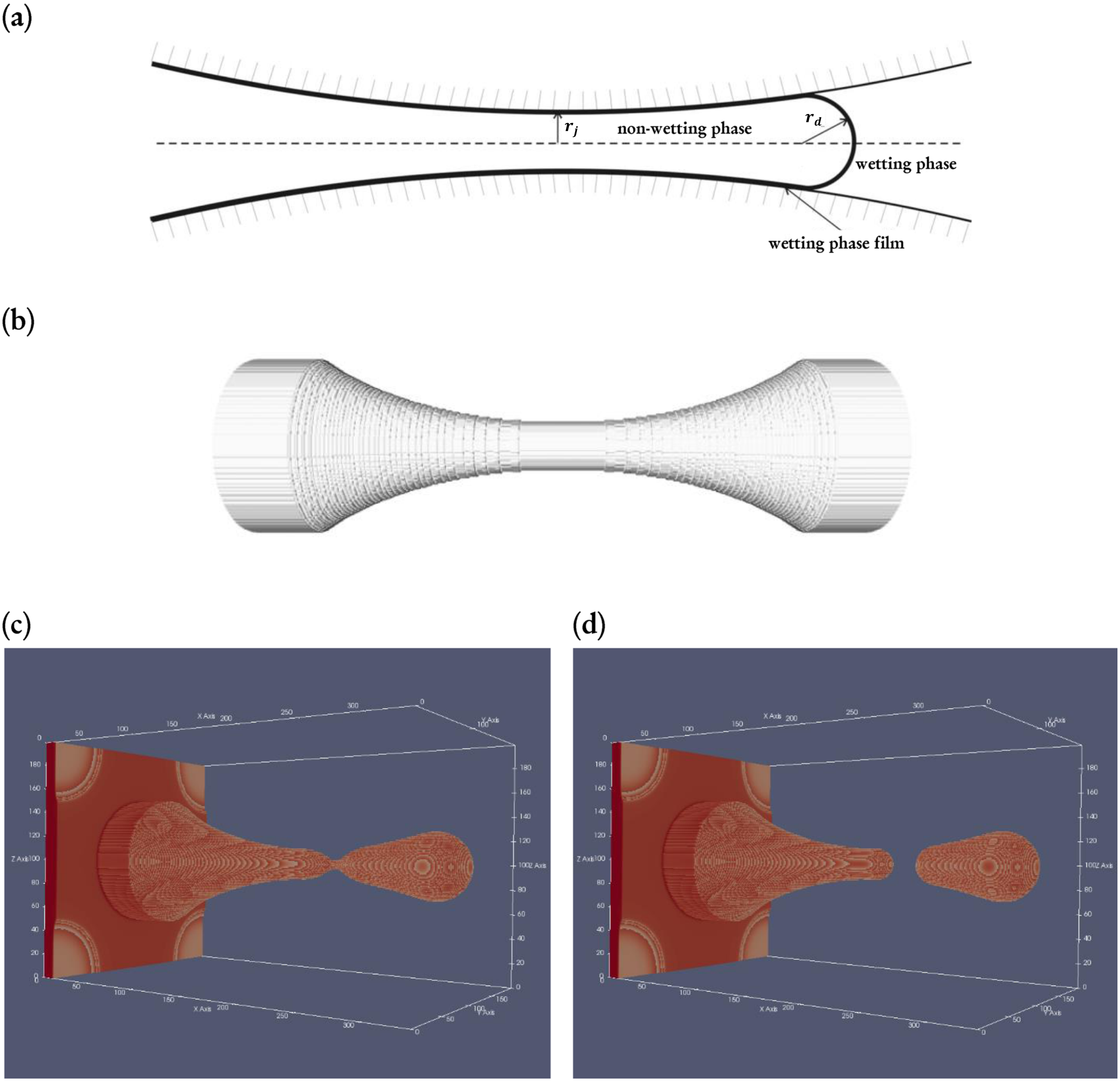

Fig. 2 **a** Schematic representation of a non-wetting fluid jet and its leading spherical interface inside a constricted capillary tube [9]. **b** Example numerical approximation of the constricted capillary tube geometry (3D view). **c** 3D numerical simulation of a non-wetting fluid jet and its leading spherical interface inside a constricted capillary tube prior to the snap-off phenomenon and **d** subsequent to the snap-off phenomenon. Phase 2 is shown in red, and solid surfaces and Phase I are transparent in the bottom figure frames

where $\varpi_f = 1/\tau_f$ is related to the fluid viscosity by Eq. 16. The zero values correspond to conserved quantities for which the relaxation time was set to infinity. This is an arbitrary choice because, independent of the relaxation parameters for these quantities, they are collision invariants since by definition $\mathbf{M}_{ji}\left[f_i - f_i^{eq}\right] = 0$ for $j = 0, 3, 5, 7$. Finally, the choice of unity for the nonhydrodynamic modes minimizes spurious velocities [79].

The benefits of the MRT model over the conventional single-relaxation-time Bhatnagar-Gross-Krook (BGK) model are (I) enhanced numerical stability, (II) independent bulk and shear viscosities, and (III) viscosity-independent, nonslip boundary conditions. The drawback of the MRT model is that it is slightly more computationally demanding compared to the BGK model. This minor hurdle is easily overcome through a general-purpose graphics

Fig. 3 Geometry-related snap-off for Model C (n_w/n_{nw} = 1.0). Snapshots of the order-parameter field are shown immediately before and after the snap-off. Red: Non-wetting phase (Phase 2); Blue: Wetting phase (Phase 1)

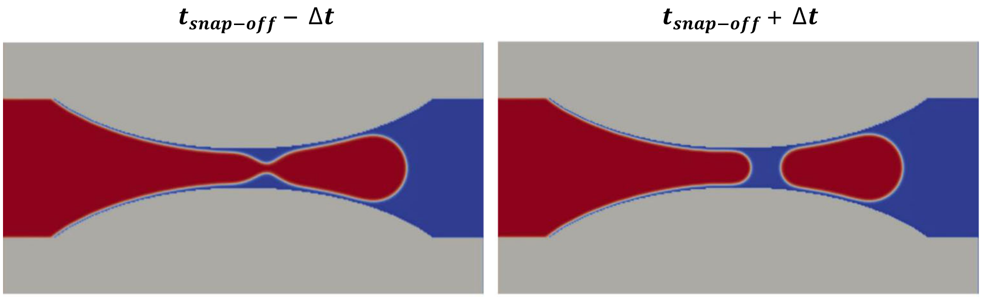

processing unit (GPGPU) implementation of the MRT model for eLBM.

2.6 Parallel implementation

The collision and propagation kernels of eLBM lend themselves very well to many lightweight computation threads provided by GPGPUs. In fact, the entire eLBM algorithm is implemented for NVIDIA GPGPU cards by the use of the Compute Unified Device Architecture (CUDA) programming language, which is a variant of the C++ programming language with extra functions to control the device (GPGPU) from the host (CPU). In addition, the eLBM code utilizes a 1D decomposition scheme with a single ghost layer communicating the solutions along domain boundaries. The domain decomposition communications are managed by the use of message passing interface (MPI).

3 Fundamental validation tests

We focus on fundamental validation tests to demonstrate the physical consistency of our direct two-phase visco-capillary flow simulator. Dynamic problems are investigated where the physical rigor of two-phase transport, mass, and momentum balance solvers are tested altogether against theoretical solutions and experimental data. Investigations of geometry-constrained snap-off in a constricted capillary tube, Haines jumps in a micromodel, Haines jumps in real rock images, and capillary desaturation in a real rock image constitute the problems investigated in this section.

3.1 Investigations of geometry-constrained snap-off

Geometry-constrained snap-off occurs in porous medium flows in narrow constrictions (pore throats) where the non-wetting phase is disconnected by swelling of wetting films. It occurs in imbibition and drainage processes. The investigated case in this paper follows closely the work by Roof [85], where the non-wetting phase snaps off in a circular capillary with a constriction. A schematic representation of the non-wetting fluid jet is shown in Fig. 2a (adapted from Armstrong et al. [9]). Previously, simulations of a similar problem have been performed using an axisymmetric formulation and the computational fluid dynamics software by Beresnev et al. [16] and Beresnev and Deng [15]. Recently, Roman et al. [84] reported measurements and simulation of liquid films during drainage displacements and snap-off in constricted capillary tubes.

Five 3D models of a constricted capillary tube geometry are generated. Each model is composed of 381 × 200 × 200 cubic cells (Fig. 2b). The voxel size is uniform and is equal to 1 μm for each model. This gives rise to a domain with a size of 3.81 mm × 2.0 mm × 2.0 mm for each model. The radius of the constriction (r_j) is varied across the model ensemble, but the domain dimensions are kept constant. The r_j values considered for Model A, Model B, Model C, Model D, and Model E are 25 μm, 20 μm, 15 μm, 10 μm, and 7 μm, respectively. Initially, the models were filled with Phase 1, which uniformly wets the entire solid surface. We impose a 0° equilibrium contact angle boundary condition on the internal surfaces of the constricted capillary

Fig. 4 Geometry-related snap-off for Model C (n_w/n_{nw} = 3.0). Snapshots of the order-parameter field are shown immediately before and after the snap-off. Red: Non-wetting phase (Phase 2); Blue: Wetting phase (Phase 1)

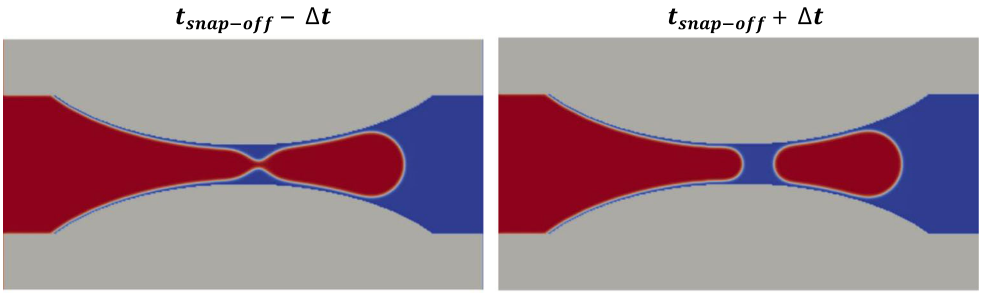

Fig. 5 Geometry-related snap-off for Model E (n_w/n_{nw} = 1.0). Snapshots of the order-parameter field are shown immediately before and after the snap-off. Red: Non-wetting phase (Phase 2); Blue: Wetting phase (Phase 1)

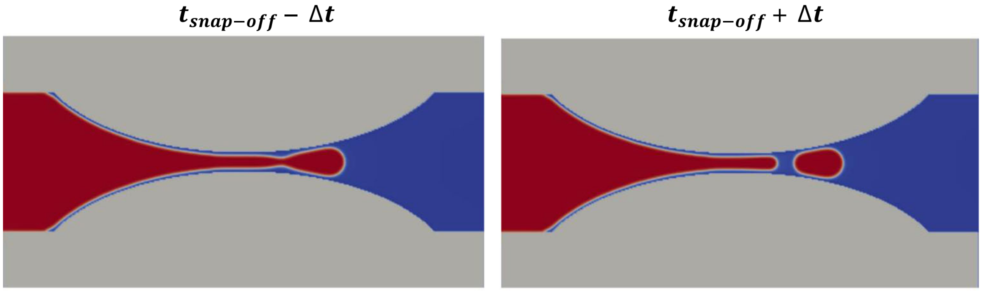

tube which corresponds to a strong water-wet solid surface. Buffer layers of 16 lattice units (l.u.) are added to the inlet and outlet of the domain to impose a constant velocity injection boundary condition at the inlet buffer. Phase 2 (Fig. 2c, d) was injected from the left side of the model very slowly with a head gradient that is close to zero to make the dynamic effects as small as possible. The capillary number of the non-wetting phase (Ca_{nw}) varies between 1.2×10^{-4} and 1.8×10^{-4} from Model A to Model E.

The first set of simulations is performed using a viscosity-matched pair of fluids ($\eta_w \big/ \eta_{nw}$=1.0) for all models. Snapshots of the order-parameter field in the center cross-section are shown immediately before and after the snap-off in Figs. 3 and 5 for Model C and Model E, respectively. Model C and Model E are also simulated for a viscosity ratio of $\eta_w \big/ \eta_{nw}$=3.0 (slightly unfavorable viscosity ratio displacement) with corresponding center cross-sectional order-parameter snapshots shown in Figs. 4 and 6, respectively. We will discuss these results later in the paper.

Roof [85] describes the mechanism, provides experimental results, and presents a simplified theoretical model for snap-off. The energy balance considerations under quasi-static conditions, i.e., without considering dynamic effects and viscous pressure drops, lead to the conclusion that snap-off occurs in the constriction of the capillary tube when the radius of the detaching drop is approximately two times larger than the radius of the non-wetting-phase stream in the constriction [9, 85]. As shown in Figs. 3, 4, 5 and 6, the stream inside the constriction has a near cylindrical shape, with one curvature radius (r_c) signifying that the capillary pressure is equal to p_c=$\gamma_{AB} \big/ r_c$. On the other hand, the detaching droplet has a near spherical shape, leading interface with two identical curvature radii (r_b). Therefore, the capillary pressure of the detaching droplet is p_b=$2\gamma_{AB} \big/ r_b$. The detachment can only occur when $p_b \le p_c$, which entails that a separate droplet is more energy favorable since it has less pressure.

We compute the roof energy balance snap-off criterion [9] for each model by using the order-parameter snapshots taken right before and after the snap-off (Fig. 7). The straight dashed line in Fig. 7 corresponds to the quasi-static energy balance criterion r_b= $2r_c$ discussed above. Overall, the relationship between the detaching drop radius in the numerical simulation (r_b) and the radius of the jet inside the constriction (r_c) honors the theoretical trend well. The correspondence seems to be best for not too narrowly and not too widely constricted capillary tubes (Model B and Model C) among the investigated models. In more narrowly constricted tubes (e.g., Model E), it can be argued the numerical discretization errors in the narrowest portion of the tube are larger compared to the other models. On the other hand, in less narrowly constricted tubes (e.g., Model A), it becomes more difficult to accurately capture the subtle curvature of the converging-diverging surfaces over a domain length that is kept constant across the model ensemble. It is important to note that the energy balance criterion is a quasi-static approximation and, as such, does not account for inertial effects. As also highlighted by DiCarlo et al. [32] and Armstrong et al. [9], snap-off is a rapid process with Re>1, while the viscous friction governs the deformation of the interface. Thus, it is not

Fig. 6 Geometry-related snap-off for Model E (n_w/n_{nw} = 1/3). Snapshots of the order-parameter field are shown immediately before and after the snap-off. Red: Non-wetting phase (Phase 2); Blue: Wetting phase (Phase 1)

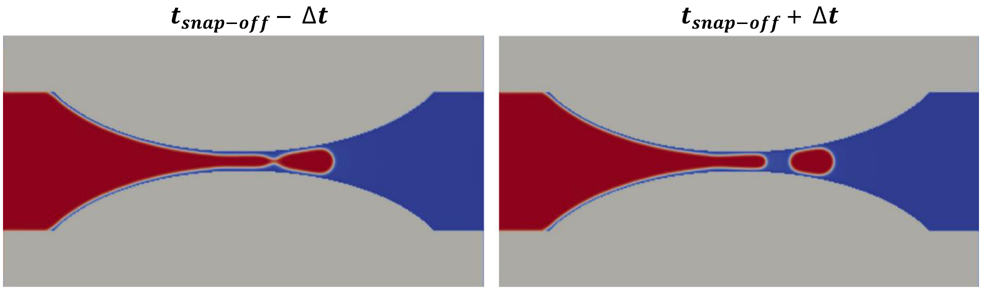

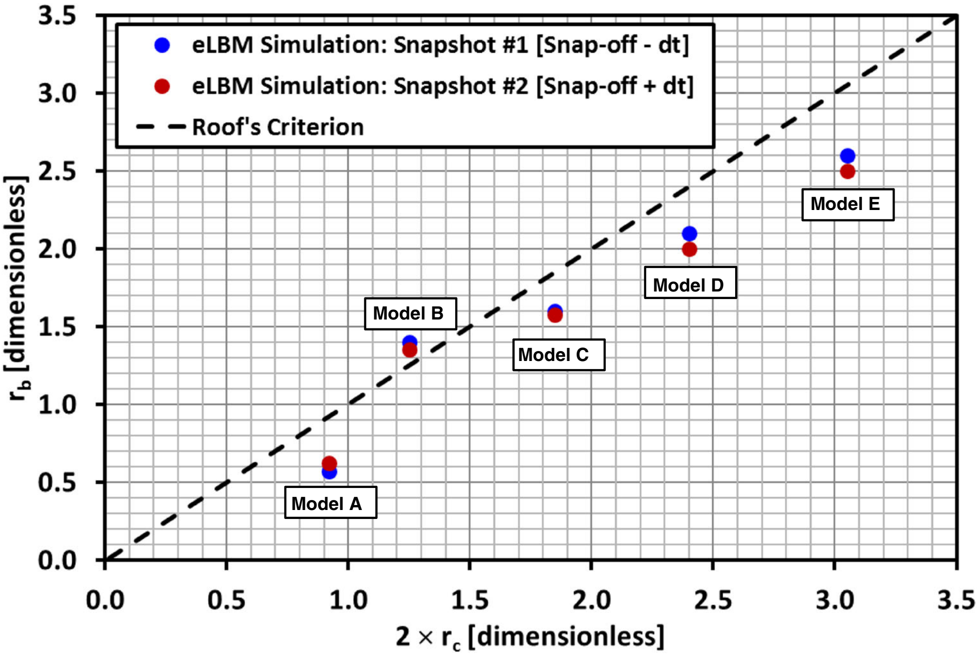

Fig. 7 Comparison of the eLBM simulation results (red and blue dots) against the quasi-equilibrium energy balance snap-off criterion by Roof (dashed line) for drainage

reasonable to expect an exact correspondence between the numerical simulation results that are based on the full-physics description of the fluid dynamics and the quasi-static energy balance criterion.

An additional set of simulations was carried out for an unfavorable viscosity ratio case with η_w / η_{nw}=3.0 for Model C and Model E and a favorable viscosity ratio case with η_w / η_{nw}=0.33 for Model C. Snapshots of the order parameter field are shown immediately before and after the snap-off in Fig. 4 for Model C and in Fig. 6 for Model E for unfavorable viscosity ratio simulations. It has been observed that snap-off consistently occurs slightly earlier for the unfavorable viscosity ratio cases because of the inherent increased tendency for viscous fingering.

In Figs. 3 and 5, it has been observed that snap-off takes place slightly off-center in the constricted capillary tube for the viscosity-matched pair of fluids. For snap-off to occur, two fundamental phenomena should take place: pressure outside the non-wetting phase (Phase 2) should be larger than the pressure inside, which is a function of curvatures and the constriction radius. However, one also needs the wetting phase to flow fast enough to allow the snap-off to happen. When the non-wetting phase (Phase 2) retracts, the wetting phase (Phase 1) has to follow. However, this interplay between non-wetting and wetting phases is not instantaneous. Thus, based on the pressure argument, necking should start at the narrowest part of the constriction; however, this is only a quasi-static argument. Under dynamic conditions, there are two arguments explaining the snap-off phenomenon occurring off-center: (1) because of the mobility limitation of the wetting-phase flow, the point where one can observe necking to really proceed is already off-center, and (2) the snap-off occurs when the necking progresses, which takes time; i.e., during the necking, which is perpendicular to the main flow direction, the main flow moves the necking point downstream.

3.2 Investigations of Haines jumps during drainage in a micromodel

Pore drainage events occur as a cooperative phenomenon, which has been postulated [74] and inferred from indirect data [40] and, more recently, proven with direct evidence [17]. The visualization of transient dynamics of Haines jumps in 2D micromodels provides clear evidence to the cooperative behavior of pore drainage events.

When a pore body is drained, retraction of nearby menisci occurs, which supplies the volume of fluid required for the drainage event. The drainage is driven by the difference in capillary pressure at the front (wide pore = small curvature) and the nearly constantly high capillary pressure in the meniscus. During this process, the elastic energy initially stored in the meniscus is converted into kinetic energy [73] which is largely dissipated by viscous forces until a new capillary equilibrium is reached and fluid is temporarily static. In this way, the pore-scale flow can be categorized into rapid (only few millisecond duration), irreversible events (Haines jump, “rheon”) [74] and much slower (lasting a few seconds) laminar-flow phases where the menisci are recharged to the same curvature/pressure before the Haines jump (“subison”) and further increased (“rison”) [99] until the pore entry pressure of the next pore system is exceeded and another Haines jump occurs.

We investigate the dynamics of Haines jump events [45], which can occur during drainage. Whether the drainage process can be considered as a cascade of events where the pore space is invaded by a non-wetting fluid pore-by-pore while neglecting the dynamics of the process to simplify the modeling work has been increasingly questioned. Pore network modeling, which takes advantage of a decomposition of the pore space into an ensemble of geometric shapes that drain in a sequential manner, based on the capillary entry pressures, neglects dynamical effects at the pore scale. However, dynamical effects due to pore-scale instabilities can alter the displacement pathways [37] or lead to fluid redistribution at a time scale comparable to the time scale of general advancement of fluid front propagation [8], and hence, the quasi-static approach used in pore network modeling may not be able to predict correctly the residual saturation after drainage and imbibition processes. Recently, Armstrong and Berg [8] and Berg et al. [18] demonstrated that capillary or viscous forces may not be acting in a purely local way. In light of this finding, the importance of considering the full dynamics at the pore scale for modeling displacement processes becomes even more apparent.

The pressure generally increases steadily during drainage. However, as the non-wetting phase travels through a narrow throat to a wider pore body because it exceeds the capillary entry pressure, the pressure drops instantaneously and the pore space fills quickly. Recent developments in synchrotron-based X-ray micro-computed tomography improved the temporal resolution in the range of seconds, enabling the imaging of pore-scale displacement events while maintaining the flow, the pressure gradients, and the visco-capillary balance during imaging [18]. This offers the possibility to directly visualize rapid events, such as the Haines jumps, and other pore-scale displacement events in porous rock real time. These rapid events are very important to the upscaling of multiphase flow since they account for a significant fraction of the energy dissipation within the system [18, 87]. Moreover, although often questioned as an irreversible displacement process, they may also contribute to macroscopic properties of the rock such as the relative permeability [75].

We investigate whether the eLBM can capture the dynamics of Haines jumps. Figure 8 shows the geometry used in 3D simulations adapted from Zacharoudiou and Boek [100]. Velocity boundary conditions are applied in the inlet and outlet of the simulation domain (in the x direction) to drive the flow, while periodic boundary conditions are imposed in the vertical (y) direction. In the z direction, walls are located at $z=0$ and $z=h$. In order to drive the drainage process, the injected non-wetting phase enters the simulation at a given flow rate $Q=\iint_A \mathbf{u}\cdot d\mathbf{A}$ at the inlet, while imposing the same flow rate at the outlet allows the wetting phase to exit the system. The geometry is an effective Hele-Shaw cell with walls located at $z=0$ and $z=h=10$ l.u. The platelets are of diameter $(d_p)=60$ l.u., representing the wider pore bodies. Six throats of width $(d_t)=12$ l.u. and length $(l_t)=22$ l.u. connect the pore bodies. Small reservoirs with a length of 16 l.u. are added at the inlet and the outlet. Simulations were performed using fluids of the same viscosity. In the first simulation, the equilibrium contact angle was set to $\theta^{eq}=30°$. The inlet fluid velocity $\left(u_x^{inlet}\right)$ was 1.0×10^{-5} l.u. The injected

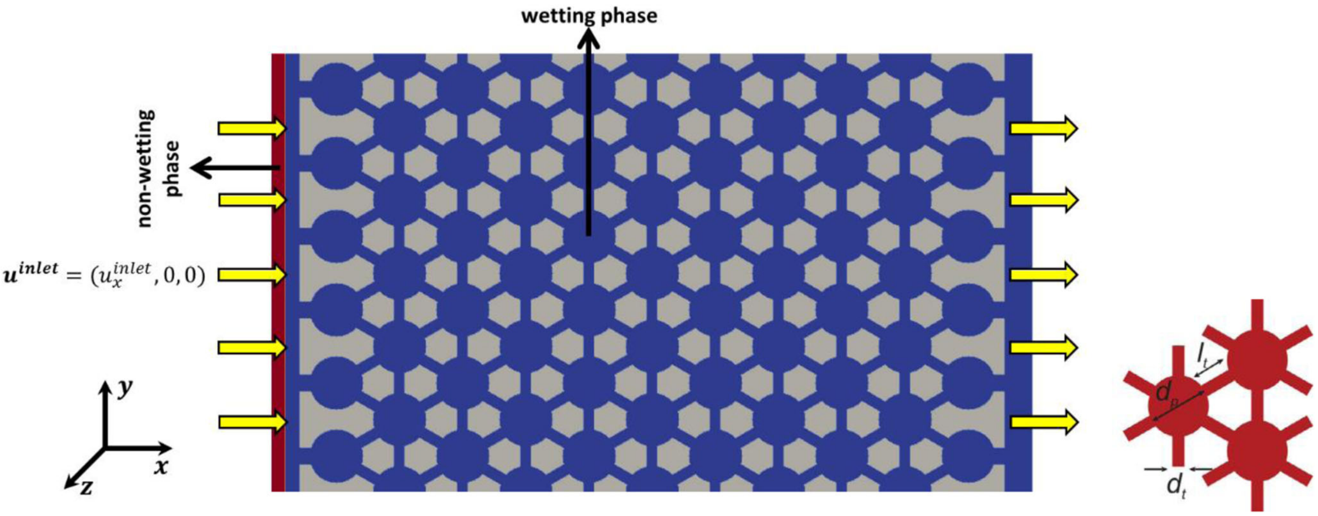

Fig. 8 The micromodel used to capture the Haines jumps. Velocity boundary conditions are applied at the inlet and outlet of the simulation domain to drive the flow, while periodic boundary conditions are imposed on the top and bottom faces of the domain. In the z direction, walls are located at $z=0$ and $z=h$. In-situ wetting phase (Phase 1): blue; Injected non-wetting phase (Phase 2): red

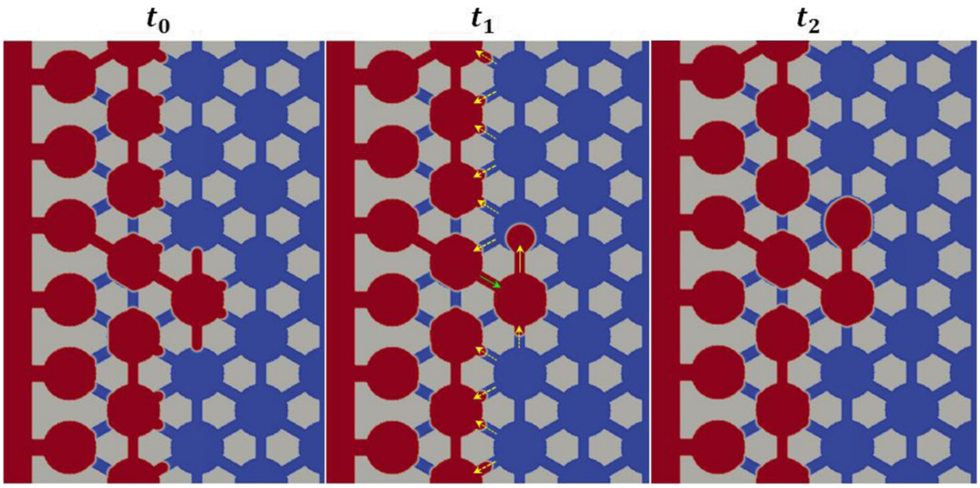

Fig. 9 Illustration of Haines jump events during drainage (Sequence #1). Pore drainage events are labeled with continuous yellow arrows. Meniscus recession is labeled with dotted yellow arrows. The flow direction is labeled with continuous green arrows. The fluid phases have the same viscosity $n_w = n_{nw} = 1.67 \times 10^{-2}$. Interfacial tension is $\sigma = 1.17 \times 10^{-2}$ l.u. Equilibrium contact angle is $\theta^{eq} = 30°$. Inlet velocity is $\mathbf{u}_{inlet} = 1.0 \times 10^{-5}$ l.u. In-situ wetting phase (Phase 1): blue; Injected non-wetting phase (Phase 2): red

non-wetting phase (Phase 2) and the in situ wetting phase (Phase 1) are viscosity and density matched. Figures 9 and 10a show two simulated order-parameter snapshot sequences during drainage. The frames of these figures illustrate the pore drainage and meniscus recession events observed during Haines jumps. The events shown in Figs. 9 and 10a have different fluid distributions prior to the Haines jump event. The first column in these figures corresponds to the beginning of the events (t=t_0), the second one corresponds to the time of maximum interfacial velocity (t=t_1), while the third one corresponds to the time when all the non-wetting fluids from the surrounding pore throats were provided for draining the pore body (t=t_2) and marked the end of fluid rearrangement during a Haines jump event.

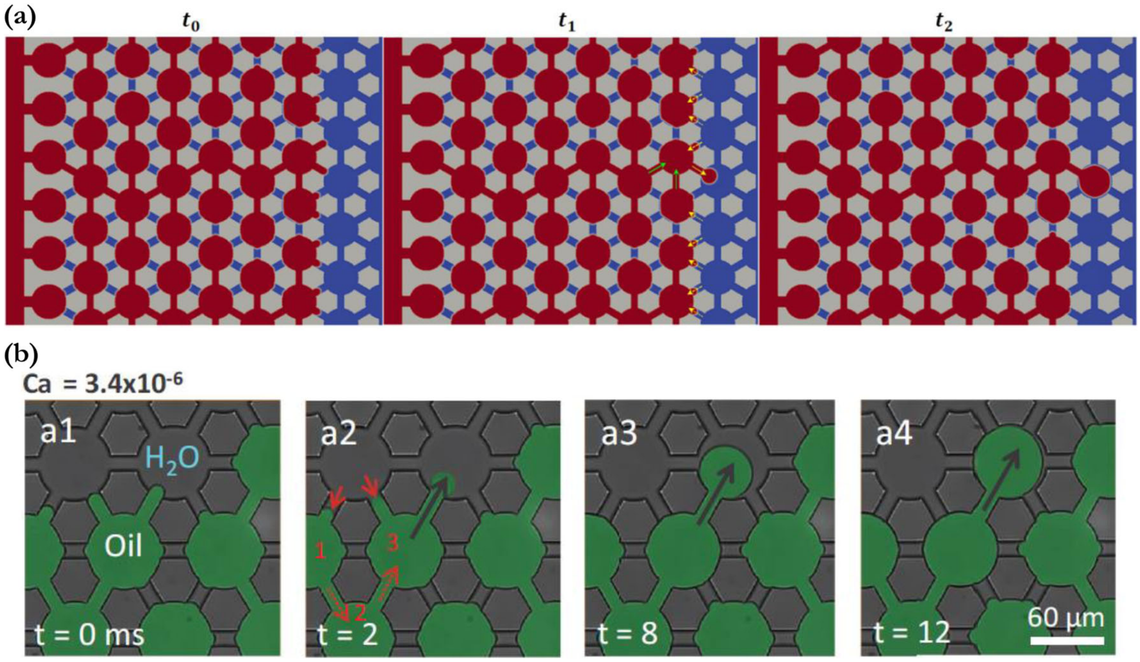

Fig. 10 **a** Illustration of Haines jump events during drainage (Sequence #2). Pore drainage events are labeled with continuous yellow arrows. Meniscus recession is labeled with dotted yellow arrows. The flow direction is labeled with continuous green arrows. The fluid phases have the same viscosity $n_w = n_{nw} = 1.67 \times 10^{-2}$. Interfacial tension is $\sigma = 1.17 \times 10^{-2}$ l.u. Equilibrium contact angle is $\theta^{eq} = 30°$. Inlet velocity is $\mathbf{u}_{inlet} = 1.0 \times 10^{-5}$ l.u. In-situ wetting phase (Phase 1): blue; Injected non-wetting phase (Phase 2): red. **b** High speed images (2,000 fps) of pore drainage events. Pore drainage events are labeled with black arrows, meniscus retraction is labeled with a red arrow, and the presumed flow direction is labeled with dotted red arrows. The figure is adapted from [8]

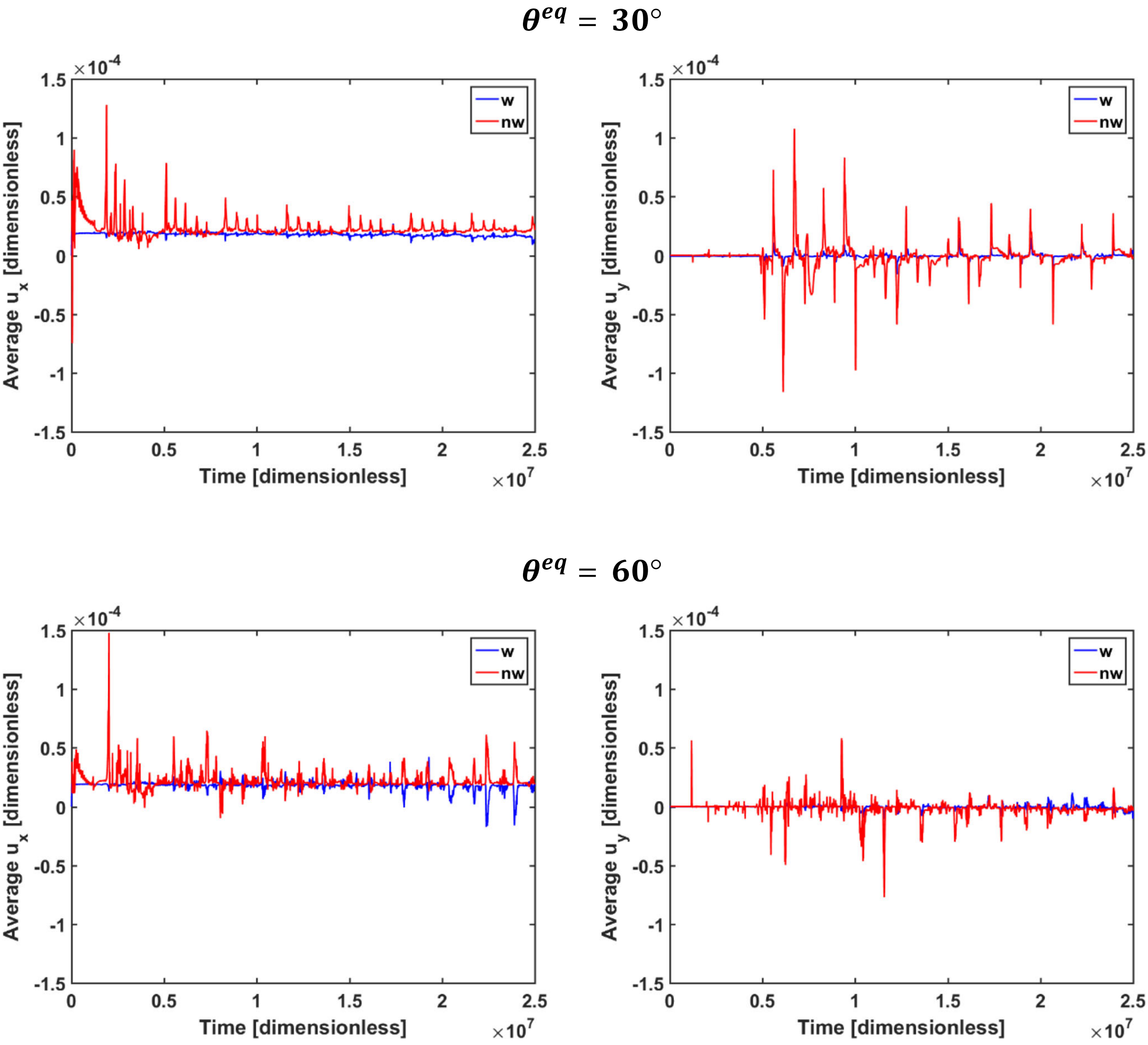

Fig. 11 The average components of the velocity vector (**u**) during drainage separately plotted for wetting (w) and non-wetting (nw) phases for $\theta^{eq} = 30°$ (top frames) and $\theta^{eq} = 60°$ (bottom frames)

During the drainage of a pore body, imbibition occurs in the neighboring throats and the fluid interface retracts. These imbibition events provide a fraction of the fluid necessary for draining the pore body and lead to rearrangement of the fluids in the surrounding area of a pore drainage event. When the non-wetting fluid reaches the wider pore body and the pressure exceeds the pore entry pressure, the interface “jumps” into the pore body, accelerating until it reaches a maximum velocity (t=t_1) and then decelerates. This initial acceleration is due to the viscous resistance of the resident wetting fluid in the pore body and inertial forces being too small to resist the rapid fluid motion by capillary forces. Differences in the curvature of the meniscus in the pore body and the menisci in the surrounding throats generate high transient pressure gradients, and therefore, capillary forces act in a nonlocal way, since a capillary pressure difference can exist over multiple pores. From the energy viewpoint, the drainage process can be divided into two flow regimes: (1) when the interface moves in the pore throats and (2) when the interface moves from a throat (narrow restriction) to a wider pore body. During the first flow regime, which can be reversible and controlled by the injection flow rate, energy is stored in the menisci and the fluid columns of the non-wetting phase in the pore throats due to the work done by external forces. This energy is then released during the Haines jump event (second flow regime), converted into kinetic energy and surface energy, and dissipated. Therefore, for a given geometry and fluids, approximately the same amount of energy will be stored in the menisci and then released, irrespective of the externally imposed flow rate, leading to the same draining times [8]. eLBM simulations are in qualitative agreement with the conclusions reached by the experimental work reported in Armstrong and Berg [8] (Fig. 10b). Experimental work and eLBM simulations demonstrate that pore drainage dynamics are cooperative and nonlocal, since they extend beyond the draining pore body. We also find the correct time scale for drainage events (~10–15 ms) is also captured by eLBM, demonstrating that eLBM also correctly resolves the fast dynamics of interfaces during pore-filling events. Note that the time scale and dynamics of pore drainage events ultimately affect front propagation and fluid-phase topology during fluid displacement [8, 72, 73]. Thus, accurate simulation of the time scales and dynamics of pore-filling events is critical for any digital rock flow-physics simulation system.

We examine the flow field during a jump event reveals that the fluid-fluid interface velocity is larger than the mean fluid velocity. This can be inferred from Fig. 11 where we plot the average components of the velocity ($\mathbf{u}$) vector for wetting and non-wetting phases during drainage for $\theta^{eq}= 30°$ and $60°$, respectively, as a function of time. The peaks in average u_x and u_y, which are more easily detectable in the non-wetting-phase velocity field, indicate the Haines jumps. The main flow is in the x direction. u_z is equal to zero due to the 2D heterogeneity in the model and the solid walls located at $z= 0$, and $z=h$ thus is not plotted. Nonzero values for average u_y indicate the jumps that are perpendicular to the direction of flow, which, if averaged over longer times, are equal to zero in line with the expectation. Haines jumps are more clearly visible for the stronger wetting case ($\theta^{eq}= 30°$).

3.3 Investigations of Haines jumps using 3D rock images

3.3.1 Ketton limestone

We investigate the Haines jump events for 3D real rock images. Figure 12 shows the first geometry used for the eLBM simulations reconstructed from micro-CT images of Ketton limestone. The model size is 700 l.u. × 700 l.u. × 700 l.u. at a resolution of 4.52 μm per l.u., which corresponds to a physical system size of 3.164 mm × 3.164 mm × 3.164 mm and a porosity of 0.159. A small reservoir (16 l.u.) is added at the inlet/outlet of the domain for two-phase flow simulations. The enforced equilibrium boundary condition is $\theta^{eq}= 40°$ in all investigated cases. We first investigate a base forced-drainage case with $\eta_w/\eta_{nw}= 1.0$ and $Ca_{nw}= 3.9\times10^{-5}$ ($u_x^{inlet}= 5.0\times10^{-6}$ l.u.) (Case #1, base case). We then generate a variation case by keeping Ca_{nw} unchanged and changing the viscosity ratio to $\eta_w/\eta_{nw}=10.0$ to explore the effects of unfavorable viscosity ratio on forced drainage (Case #2). We generate a second variation case with $\eta_w/\eta_{nw}=10.0$ and $Ca_{nw}=8.6\times10^{-6}$ (Case #3) where Ca_{nw} is reduced significantly while retaining the unfavorable viscosity ratio of Case #2. The final forced-drainage variation case features a more than 1 order of magnitude increase in Ca_{nw} ($Ca_{nw}= 5.9\times10^{-4}$) while retaining $\eta_w/\eta_{nw}=1.0$ of the base case. Finally, we simulate forced imbibition starting from the end-point of forced drainage of the base case. In both base forced-drainage and forced-imbibition cases, the enforced constant inlet velocity boundary condition is kept the same at $u_x^{inlet}= 5.0\times10^{-6}$ l.u., resulting in a case with $\eta_w/\eta_{nw}= 1.0$, $Ca_{nw}= 1.7\times10^{-5}$, and $Ca_w= 2.0\times10^{-5}$.

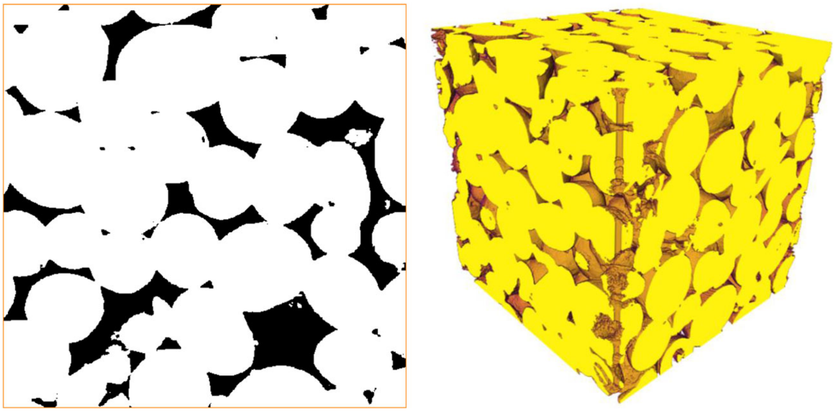

Fig. 12 Geometry used for the eLBM simulations reconstructed from micro-CT images of Ketton limestone. The model size is 700 × 700 × 700 lattice units (l.u.) at a resolution of 4.52 µm per l.u., which corresponds to a physical system size of (3.164 × 3.164 × 3.164 mm^3) and a porosity of 0.159. A small reservoir (16 l.u.) is added at the inlet/outlet of the domain for two-phase flow simulations

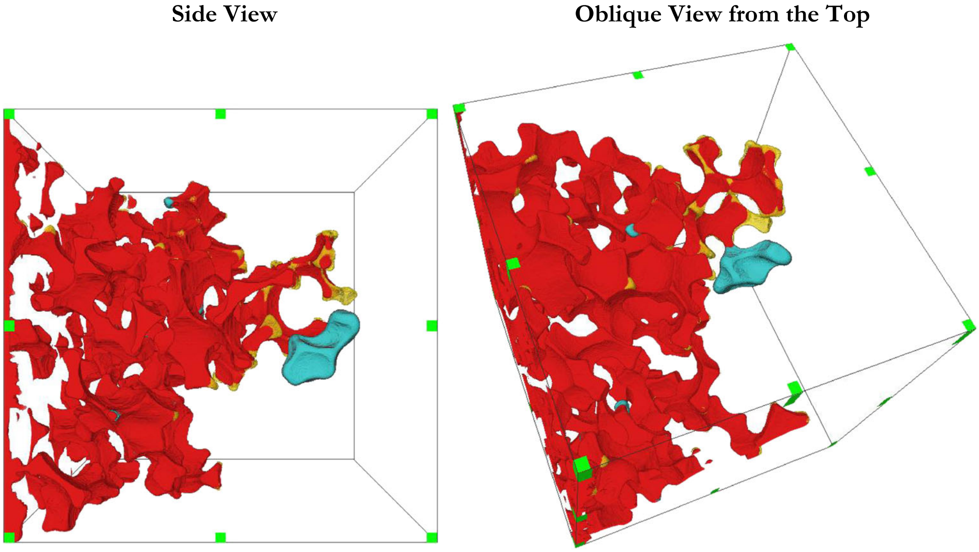

Fig. 13 Haines jump events and the associated fluid rearrangement in the Ketton limestone image. The region occupied by the non-wetting phase that remains unchanged before and after the jump event is shown in red. The draining pore bodies where the non-wetting phase replaces the wetting phase are shown in light blue. The interfacial recession events are shown in orange. The non-wetting phase appears to be well connected indicating that imbibition sites directly provide the extra fluid volume needed for draining the pore bodies

We perform a time-lapse analysis of the order-parameter field and visualize a series of Haines jump events for the base case. Figure 13 documents these Haines jump events and the associated fluid rearrangement. The figure panels show the region occupied by the non-wetting phase that remains unchanged before and after the jump event. The draining pore body and interfacial recession are also shown. The non-wetting phase appears to be well connected, indicating that imbibition sites directly provide the extra fluid volume needed for draining the pore body.

In Fig. 14, we report pore volume–averaged velocity components for the wetting and non-wetting phases as a function of time for the investigated forced-drainage case variants and for the forced-imbibition case. The inlet and outlet reservoirs are excluded in all averaging calculations. The non-wetting-phase average velocity in the main flow direction (u_x) (Fig. 14) clearly shows the signatures of the Haines jump events for the base case (Case #1) similar to the ones observed for the micromodel study discussed in the previous section (Fig. 11). They become less pronounced for an unfavorable viscosity ratio displacement ($\eta_w / \eta_{nw}=10.0$) for the same Ca_{nw} as shown in case 3. However, when the Ca_{nw} is further reduced for the same unfavorable viscosity ratio, the Haines jump events become more pronounced as in the base case. The case with increased Ca_{nw} and base-case viscosity ratio (Case #4) indicates that the Haines jump events are suppressed as the visco-capillary flow becomes more viscous dominated than capillary dominated. Haines jump signatures are of smaller magnitude for the post-drainage forced imbibition.

For each investigated case, we calculate the average saturation for the wetting and non-wetting phases as a function of time. Results are documented in Fig. 15. For capillary-dominated lower Ca_{nw} cases, we observe a sharp transition from breakthrough to (apparent) residual wetting-phase saturation state (Case #1, Case #2, and Case #3) while transition is smoother for the high Ca_{nw} case (Case #4). The high-Ca_{nw} case leads to the lowest residual wetting-phase saturation for forced drainage in line with the expectation. The unfavorable viscosity ratio displacement leads to a slightly higher residual wetting-phase saturation as shown by the comparison of Case #1 and Case #2 also in line with the expectation. Reducing Ca_{nw} for the unfavorable viscosity ratio displacement reduces the residual non-wetting-phase saturation slightly as shown in a comparison of Case #2 and Case #3. Post-drainage and post-imbibition non-wetting-phase fluid configurations are visualized for Case #1, excluding the inlet and outlet buffers in Fig. 16.

Figure 17 shows the non-wetting-phase saturations (S_{nw}) as a function of the frontal position for the investigated forced-drainage cases. Rapid advancements of the frontal position at constant S_{nw} indicate the forward Haines jumps. On the other hand, rapid increases in the S_{nw} at constant frontal position indicate the backward Haines jumps. Forward and backward Haines jumps are much more distinct for lower Ca_{nw} cases with more capillary-dominated flows, namely Case #1 through Case #3. Case #4 features relatively more viscous-dominated flows. Thus, the signatures of Haines jumps on the S_{nw} versus frontal position function are less distinct.

Berg et al. [18] reported the pressure drop for a sequence of seven scans showing individual pore-filling events during two-phase displacement (Fig. 18a). We

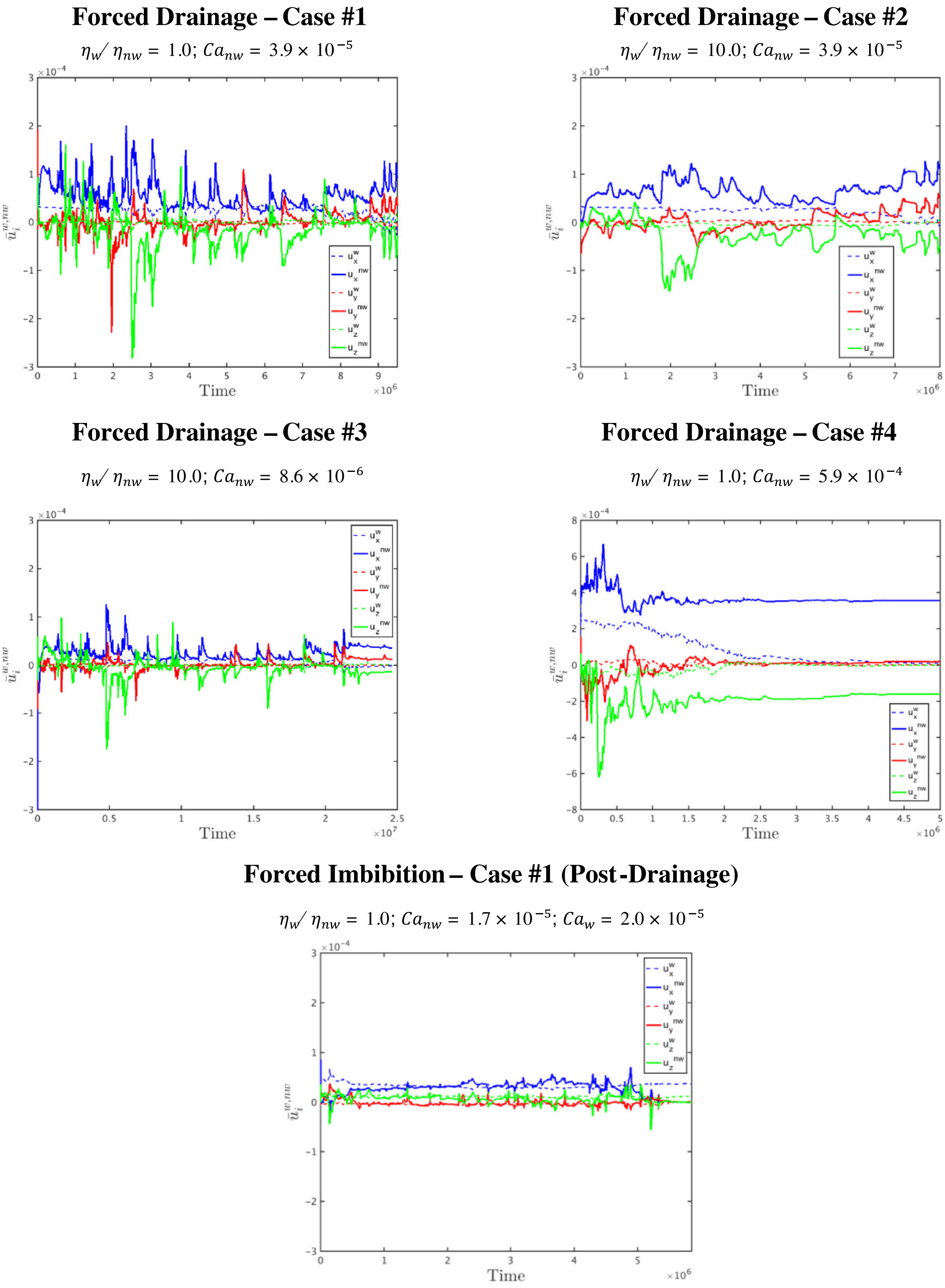

Forced Drainage – Case #1

$\eta_w / \eta_{nw} = 1.0$; $Ca_{nw} = 3.9 \times 10^{-5}$

Forced Drainage – Case #2

$\eta_w / \eta_{nw} = 10.0$; $Ca_{nw} = 3.9 \times 10^{-5}$

Forced Drainage – Case #3

$\eta_w / \eta_{nw} = 10.0$; $Ca_{nw} = 8.6 \times 10^{-6}$

Forced Drainage – Case #4

$\eta_w / \eta_{nw} = 1.0$; $Ca_{nw} = 5.9 \times 10^{-4}$

Forced Imbibition – Case #1 (Post-Drainage)

$\eta_w / \eta_{nw} = 1.0$; $Ca_{nw} = 1.7 \times 10^{-5}$; $Ca_w = 2.0 \times 10^{-5}$

Fig. 14 Average (over the pore space) velocity components for the wetting and non-wetting phases as a function of time for various forced-drainage cases and for the forced-imbibition case that starts from the end-point of Forced Drainage – Case #1. w: wetting phase; nw: non-wetting phase

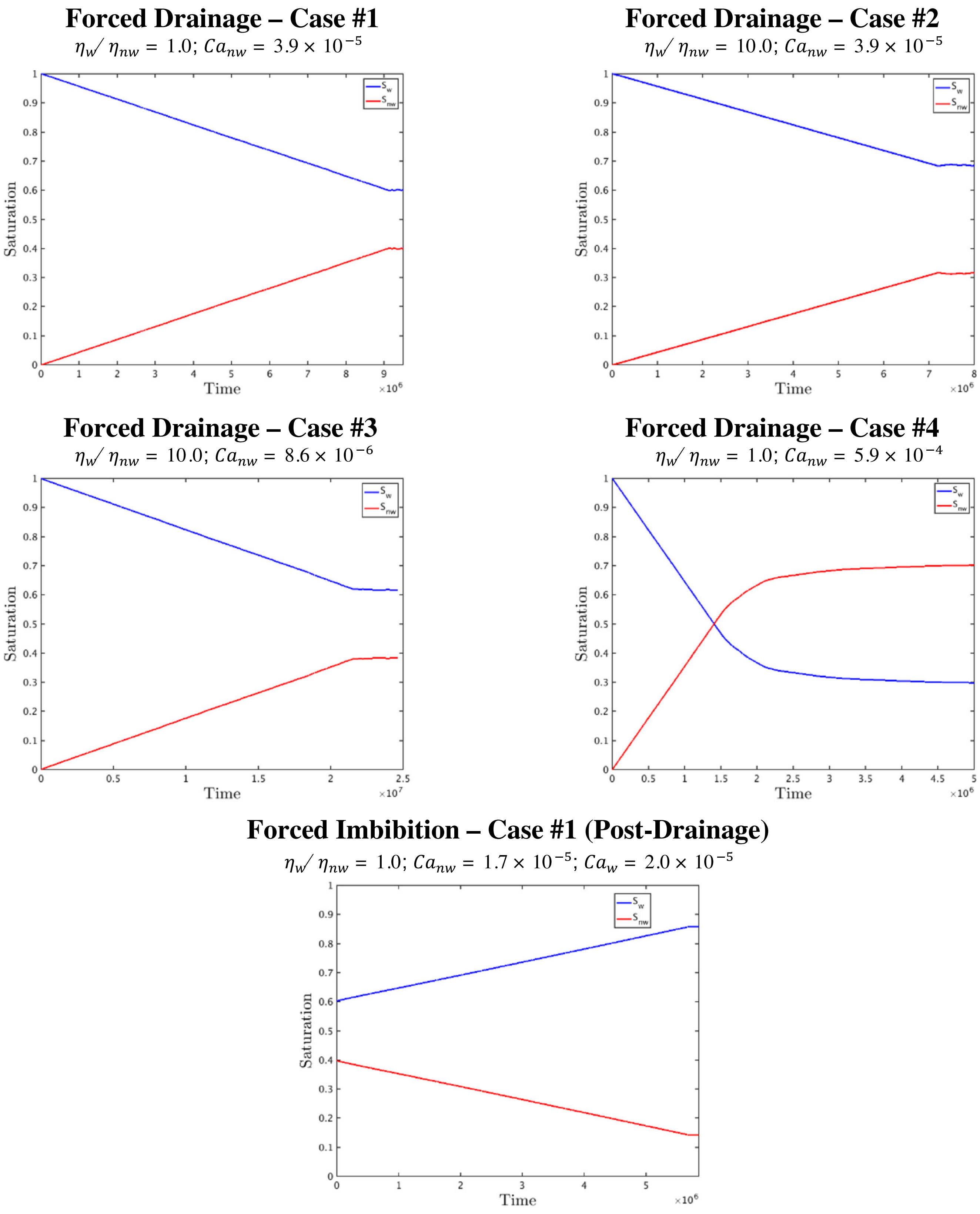
Forced Drainage – Case #1

$\eta_w/\eta_{nw} = 1.0; Ca_{nw} = 3.9 \times 10^{-5}$

Forced Drainage – Case #2

$\eta_w/\eta_{nw} = 10.0; Ca_{nw} = 3.9 \times 10^{-5}$

Forced Drainage – Case #3

$\eta_w/\eta_{nw} = 10.0; Ca_{nw} = 8.6 \times 10^{-6}$

Forced Drainage – Case #4

$\eta_w/\eta_{nw} = 1.0; Ca_{nw} = 5.9 \times 10^{-4}$

Forced Imbibition – Case #1 (Post-Drainage)

$\eta_w/\eta_{nw} = 1.0; Ca_{nw} = 1.7 \times 10^{-5}; Ca_w = 2.0 \times 10^{-5}$

Fig. 15 Average (over the pore space) saturation for the wetting and non-wetting phases as a function of time for various forced-drainage cases and for the forced-imbibition case that starts from the end-point of Forced Drainage – Case #1. w: wetting phase; nw: non-wetting phase. Buffers are not included in the saturation calculations

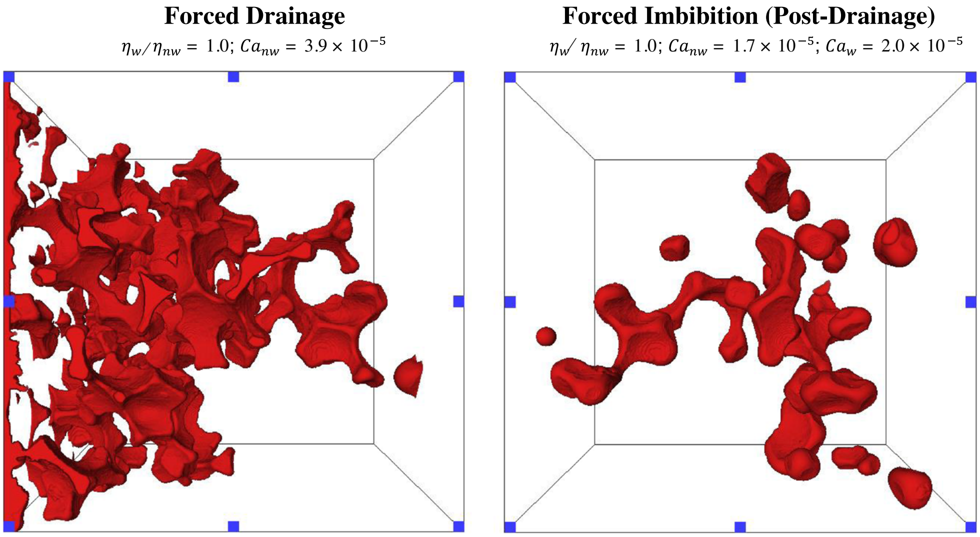
Forced Drainage

$\eta_w/\eta_{nw} = 1.0$; $Ca_{nw} = 3.9 \times 10^{-5}$

Forced Imbibition (Post-Drainage)

$\eta_w/\eta_{nw} = 1.0$; $Ca_{nw} = 1.7 \times 10^{-5}$; $Ca_w = 2.0 \times 10^{-5}$

Fig. 16 Post-drainage and post-imbibition non-wetting phase fluid configurations are visualized for the Ketton limestone image (Case #1). Inlet and outlet buffers are excluded in the visualization

compare this experimental pressure drop data qualitatively to that computed by eLBM for Case #1. Numerically simulated pressure drop data are computed by calculating the difference between average inlet and outlet pressure as a function of time and wetting-phase saturation from eLBM simulation on the Ketton limestone sample. Note that subsequent to the breakthrough, average phase pressures at the inlet becomes less meaningful, which is the behavior observed after about $t = 9\times10^6$ in Fig. 18b, which corresponds to $S_w = 0.6$ in Fig. 18c. Experimental pressure drop data and numerically simulated pressure drop results show very similar trends for capillary-dominated visco-capillary flows.

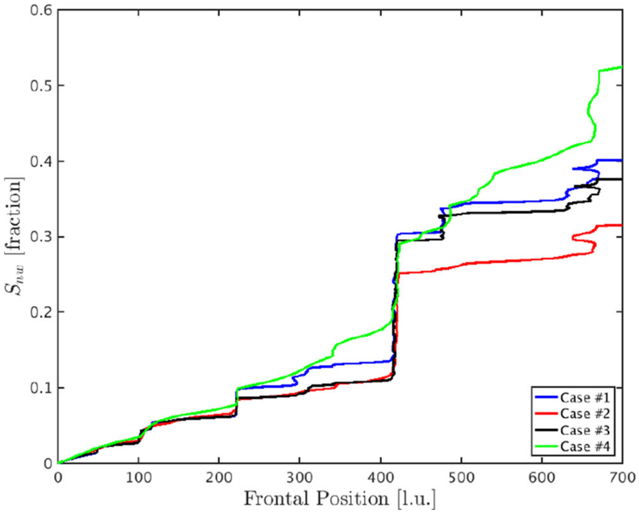

Fig. 17 Non-wetting phase saturation profiles as a function of the frontal position for the investigated forced-drainage cases

3.3.2 Fontainebleau sandstone

The second geometry used for the eLBM simulations is reconstructed from micro-CT images of Fontainebleau sandstone [5, 6] (Fig. 19). The model size is 288 l.u. × 288 l.u. × 300 l.u. at a resolution of 7.5 μm per l.u., which corresponds to a physical system size of 2.16 mm × 2.16 mm × 2.25 mm. The porosity of the image is 0.147. The computed permeabilities are 1627 mD, 1413 mD, and 1699 mD in the x, y, and z directions, respectively. The measured permeability of the much larger core sample from which the image is taken is ~1100 mD. Both forced-drainage and subsequent forced-imbibition processes are simulated with eLBM. Two-phase flow simulations are performed in the x direction. A small reservoir (16 l.u.) is added at the inlet/outlet of the domain for these simulations. The enforced equilibrium boundary condition is $\theta^{eq} = 60°$ in all investigated cases. The key dimensionless numbers are $\eta_w/\eta_{nw} = 10.0$, $Ca_{nw} = 1.7\times 10^{-5}$(forced drainage), and $Ca_{nw} = 7.7\times10^{-6}$ and $Ca_w = 7.2\times 10^{-5}$ (forced imbibition). The velocity boundary condition imposed on the inlet buffer is $u_x^{inlet} = 2.0\times10^{-6}$ l.u. for both cases.

Forced imbibition starts from the end-point of the forced drainage as described in the Ketton limestone case. The difference between average inlet and outlet pressure as a function of wetting-phase saturation is illustrated in Fig. 20 for forced-drainage and forced-imbibition processes. It is important to note that the outlet experiences two-phase flow upon injected fluid breakthrough near the end of the forced drainage process, and the pressure difference do not reflect the difference of phase pressures anymore at that time. On the other hand, the inlet buffer for forced imbibition requires a certain amount of buildup time for pressure at

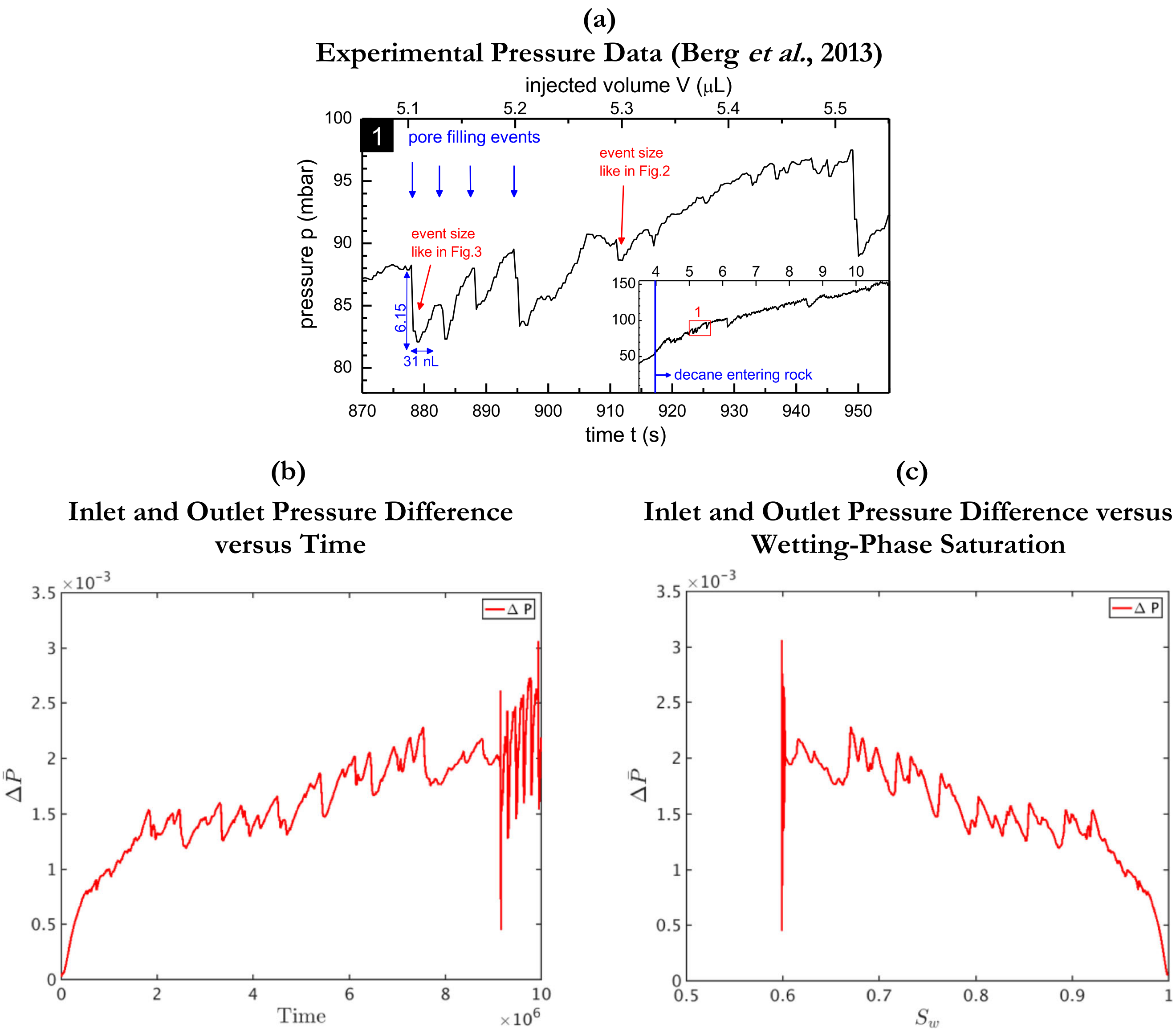

Fig. 18 Qualitative comparison of the (**a**) experimental and (**b**) numerically computed time evolution of pressure drop during two-phase displacement. The pressure drop for a sequence of seven scans showing individual pore-filling events (entire drainage experiment in the inset) reported by Berg et al. [18] (top frame). **c** Difference between average inlet and outlet pressure as a function of wetting-phase saturation from eLBM simulation on the Ketton limestone sample ($n_w/n_{nw} = 1.0$; $Ca_{nw} = 3.9 \times 10^{-5}$). Note that, in panels (**b**) and (**c**), the outlet experiences two-phase flow upon injected fluid breakthrough near the end of the forced-drainage process, and the pressure difference does not reflect the difference of phase pressures at that time (hence oscillations are observed)

the beginning of the forced-imbibition process. Therefore, it takes a while for the pressure to reflect a steady-state-like phase pressure difference.

We investigate the effect of capillary number, and hence the strength of Haines jumps, on saturation profiles for forced drainage and imbibition cycles on the Fontainebleau sandstone image. Two cases are investigated, with the first one (Case #1) being the one in the above-described study. A second case (Case #2) is generated for the same viscosity ratio with approximately 1 order of magnitude higher capillary numbers, i.e., $\eta_w \big/ \eta_{nw} = 10.0$, $Ca_{nw} = 1.5 \times 10^{-4}$(forced drainage), and $Ca_{nw} = 2.1 \times 10^{-5}$ and $Ca_w = 7.7 \times 10^{-4}$ (forced imbibition). Non-wetting-phase saturation profiles as a function of the frontal position are illustrated for the forced-drainage part of the simulations in Fig. 21. For Case #1, signatures of forward and backward Haines jumps are present, but they are weaker compared to the Ketton limestone case (Fig. 17). The magnitudes of the jumps are notably smaller, especially in the forward direction due to the more complex pore morphology. On the other hand, signatures of Haines jumps are practically absent for Case #2. Saturation for the wetting

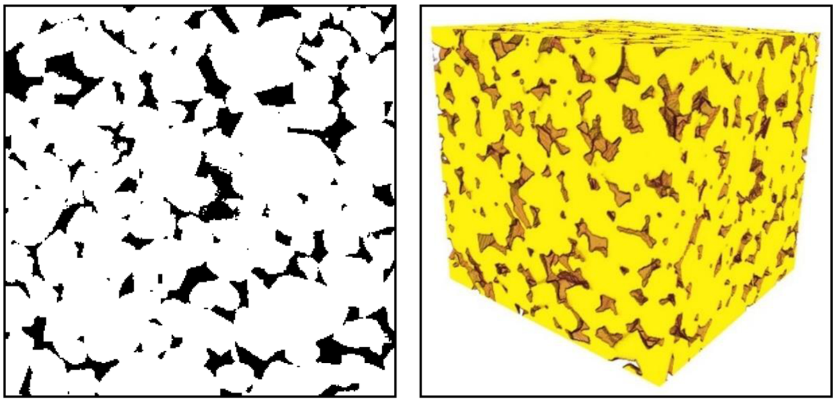

Fig. 19 Geometry used for the eLBM simulations reconstructed from micro-CT images of Fontainebleau sandstone. The model size is 288 × 288 × 300 lattice units (l.u.) at a resolution of 7.5 µm per l.u., which corresponds to a physical system size of 2.16 × 2.16 × 2.25 mm^3 and a porosity of 0.147. A small reservoir (16 l.u.) is added at the inlet/outlet of the domain for two-phase flow simulations

and non-wetting phases as a function of time are shown in Fig. 22. Moreover, post-drainage and post-imbibition non-wetting-phase fluid configurations are visualized in Fig. 23 excluding the inlet and outlet buffers for cases when the non-wetting-phase saturation in the rock is nonzero. While there is an apparent residual oil saturation of ∼0.04 for Case #1 at the end of the forced-imbibition process, for the high-capillary-number case, none of the non-wetting phase is left behind. It is important to note that buffers are not included in the saturation calculations. It is demonstrated in Figs. 22 and 23 that capillary phenomena (i.e., snap-off and Haines jumps) over drainage and imbibition cycles play a crucial role in establishing non-wetting-phase residual saturation in porous rocks. While for a high-capillary-number flow, one can place a larger saturation of the non-wetting phase during drainage, a high-capillary-number injection of the wetting phase can displace all of the non-wetting-phase saturation during a forced-imbibition event leading to a zero non-wetting-phase saturation (Figs. 22 and 23). This simulation study indicates that pore-scale simulation with eLBM can be effectively used to forecast waterflooding performance and design injection/production rates and possibly interfacial tension to reduce residual oil. A comparison of the spatial distributions of the nonwetting-phase fluid in the panels of Figs. 16 and 23 reveals the major differences between a limestone and sandstone rock, respectively. The eLBM simulator can generally handle limestone and sandstone rock if a given rock type does not contain significant microporosity in micro-CT–resolved grains.

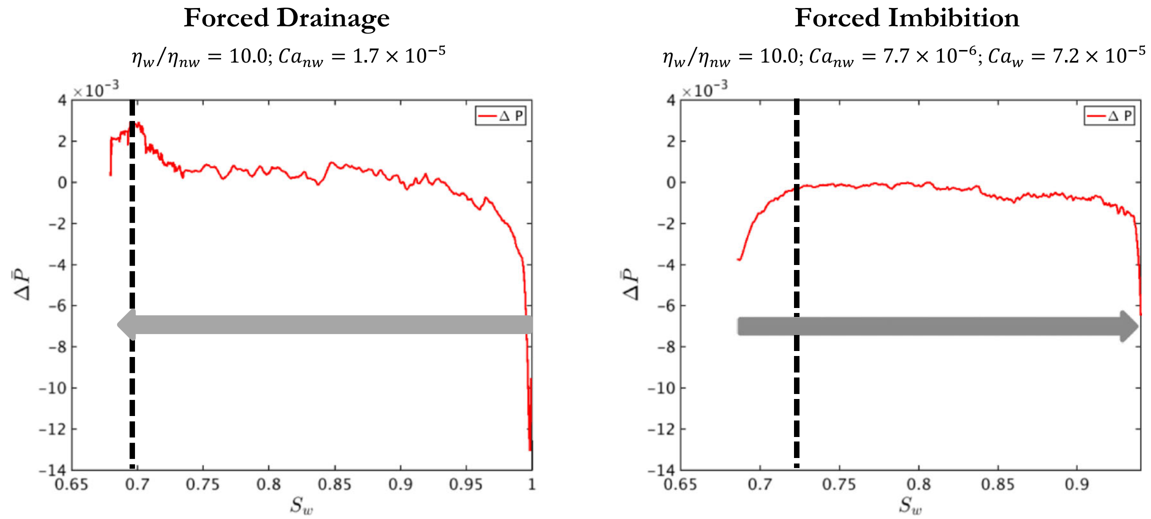

Forced Drainage

$\eta_w/\eta_{nw} = 10.0; Ca_{nw} = 1.7 \times 10^{-5}$

Forced Imbibition

$\eta_w/\eta_{nw} = 10.0; Ca_{nw} = 7.7 \times 10^{-6}; Ca_w = 7.2 \times 10^{-5}$

Fig. 20 Difference between average inlet and outlet pressure as a function of wetting-phase saturation. Forced-drainage and forced-imbibition processes are simulated with the Fontainebleau sandstone image (w: wetting phase; nw: non-wetting phase). Forced imbibition starts from the end-point of the forced drainage. The gray arrow shows the direction of the displacement process. The outlet experiences two-phase flow upon injected fluid breakthrough near the end of the forced-drainage process, and the pressure difference does not reflect the difference of phase pressures anymore at that time (left-hand side of the dashed line in the left-hand side frame). On the other hand, the inlet buffer for forced imbibition requires a certain amount of buildup time for pressure at the beginning of the forced imbibition process (left-hand side of the dashed line in the right-hand side frame). Therefore, it takes a while for the pressure to reflect a steady-state-like phase pressure difference

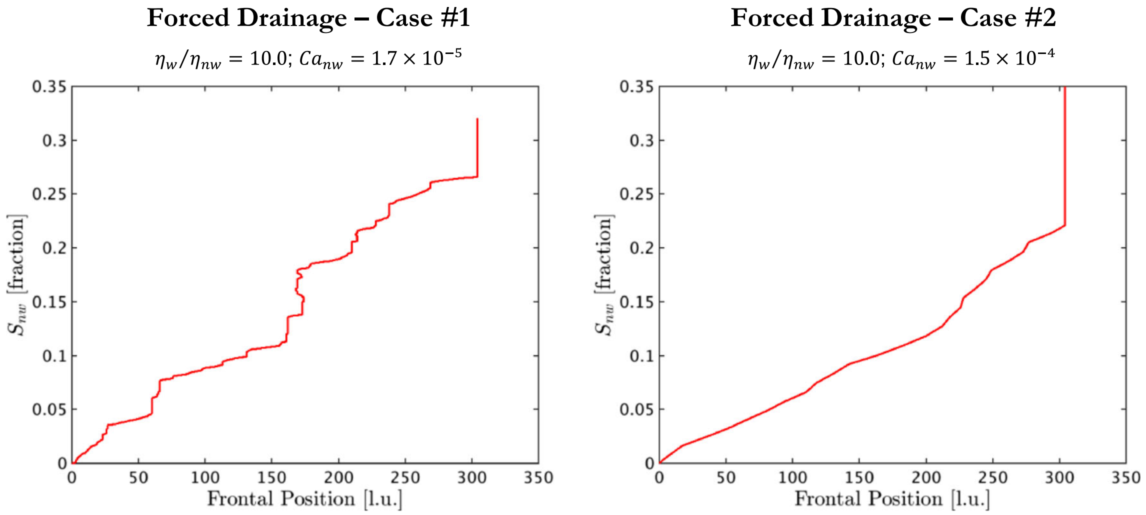

Fig. 21 Non-wetting phase saturation profiles as a function of the frontal position for the investigated Fontainebleau sandstone forced-drainage cases

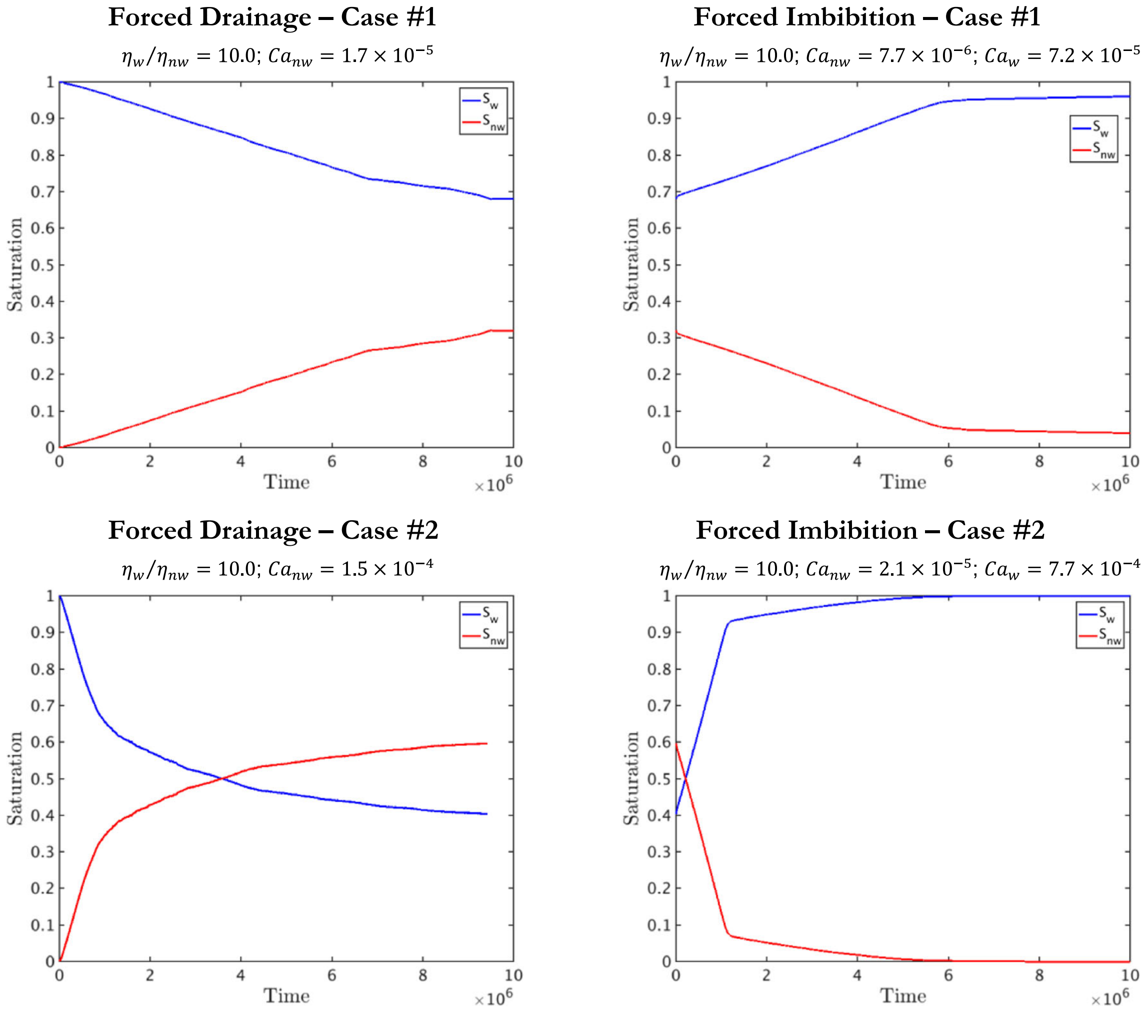

Fig. 22 The effect of capillary number on saturation profiles for a forced-drainage and forced-imbibition cycle. Two cases are investigated, and associated capillary numbers are shown together with the average (over the pore space) saturation for the wetting and non-wetting phases as a function of time. Buffers are not included in the saturation calculations

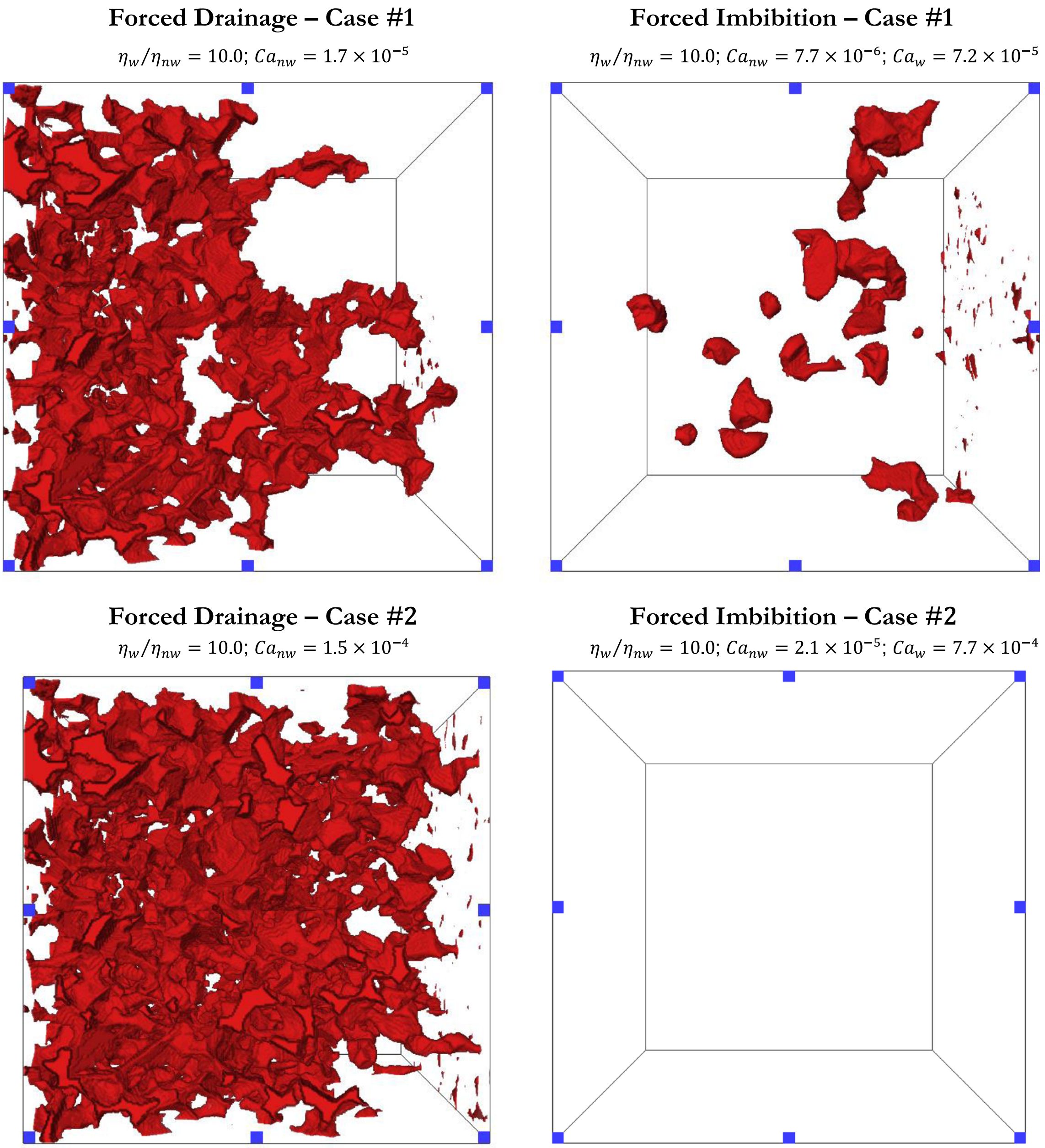

Fig. 23 Post-drainage and post-imbibition (non-zero) non-wetting phase fluid configurations are visualized for the Fontainebleau sandstone image. Inlet and outlet buffers are excluded in the visualization

3.3.3 Castlegate sandstone

The third geometry used for the eLBM simulations is reconstructed from micro-CT images of Castlegate sandstone (Fig. 24). The model size is 800 lattice units (l.u.) × 800 l.u. × 800 l.u. at a resolution of 2.072 μm per l.u., which corresponds to a physical system size of 1.66 mm × 1.66 mm × 1.66 mm and a porosity of 0.217. A small reservoir (16 l.u.) is added at the inlet/outlet of the domain for two-phase flow simulations. The enforced equilibrium boundary condition is $\theta^{eq} = 40°$ in all investigated cases. We investigate a forced-drainage case with $\eta_w / \eta_{nw} = 1.0$ and $Ca_{nw} = 3.9 \times 10^{-5}$ and a subsequent forced-imbibition case with $\eta_w / \eta_{nw} = 1.0$, $Ca_{nw} = 1.3 \times 10^{-5}$, and $Ca_w = 1.5 \times 10^{-5}$. The velocity boundary condition imposed on the inlet buffer is $u_x^{inlet} = 5.0 \times 10^{-6}$ l.u.

We perform a time-lapse analysis of the order-parameter field and visualize a series of Haines jump events for the base case. Figure 25 documents these Haines jump events and the associated fluid rearrangement. The figure panels show the region occupied by the non-wetting phase that

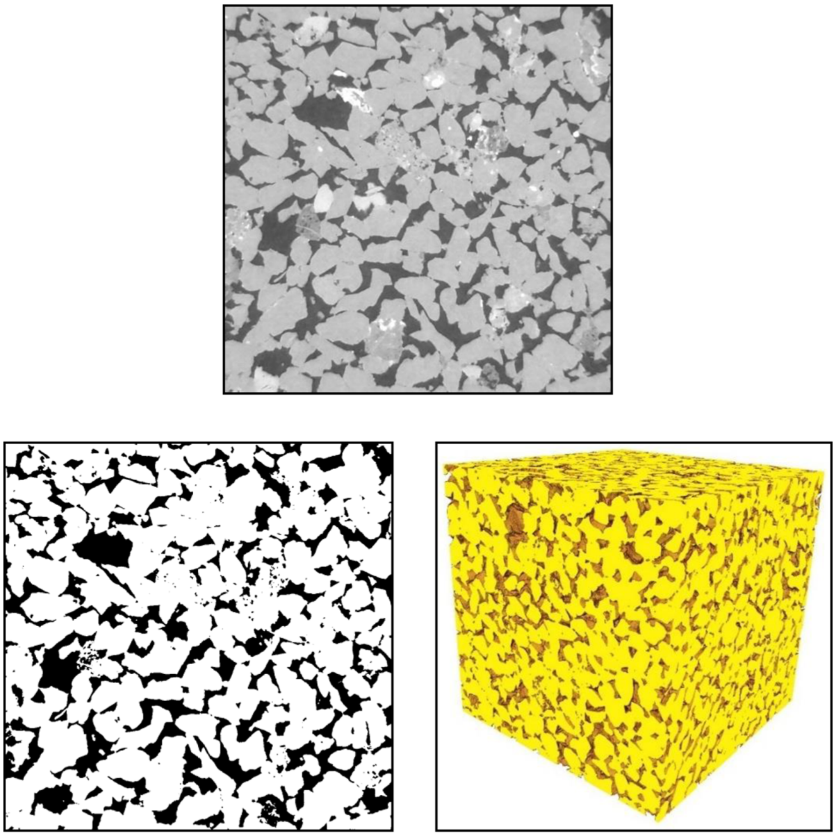

Fig. 24 Geometry used for the eLBM simulations reconstructed from micro-CT images of Castlegate sandstone. The model size is 800 × 800 × 800 lattice units (l.u.) at a resolution of 2.072 µm per l.u., which corresponds to a physical system size of (1.66 × 1.66 × 1.66 mm^3) and a porosity of 0.217. A small reservoir (16 l.u.) is added at the inlet/outlet of the domain for two-phase flow simulations

remains unchanged before and after the jump event. The draining pore body and interfacial recession are also shown. The non-wetting phase appears to be well connected, indicating that imbibition sites directly provide the extra fluid volume needed for draining the pore body.

Average (over the pore space) velocity components for the wetting and non-wetting phases as a function of time are illustrated in Fig. 26a for forced-drainage and forced-imbibition processes. Castlegate sandstone has a more complex pore space than the Ketton limestone. Haines

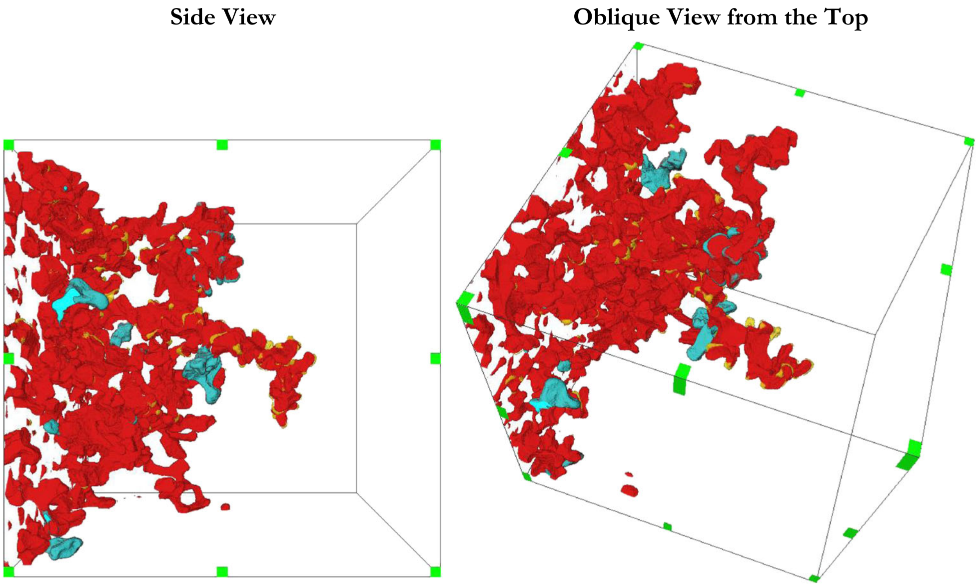

Side View

Oblique View from the Top

Fig. 25 Haines jump events and the associated fluid rearrangement in the Castlegate sandstone image. The region occupied by the non-wetting phase that remains unchanged before and after the jump event is shown in red. The draining pore bodies where the non-wetting phase replaces the wetting phase are shown in light blue. The interfacial recession events are shown in orange. The non-wetting phase appears to be well connected indicating that imbibition sites directly provide the extra fluid volume needed for draining the pore bodies

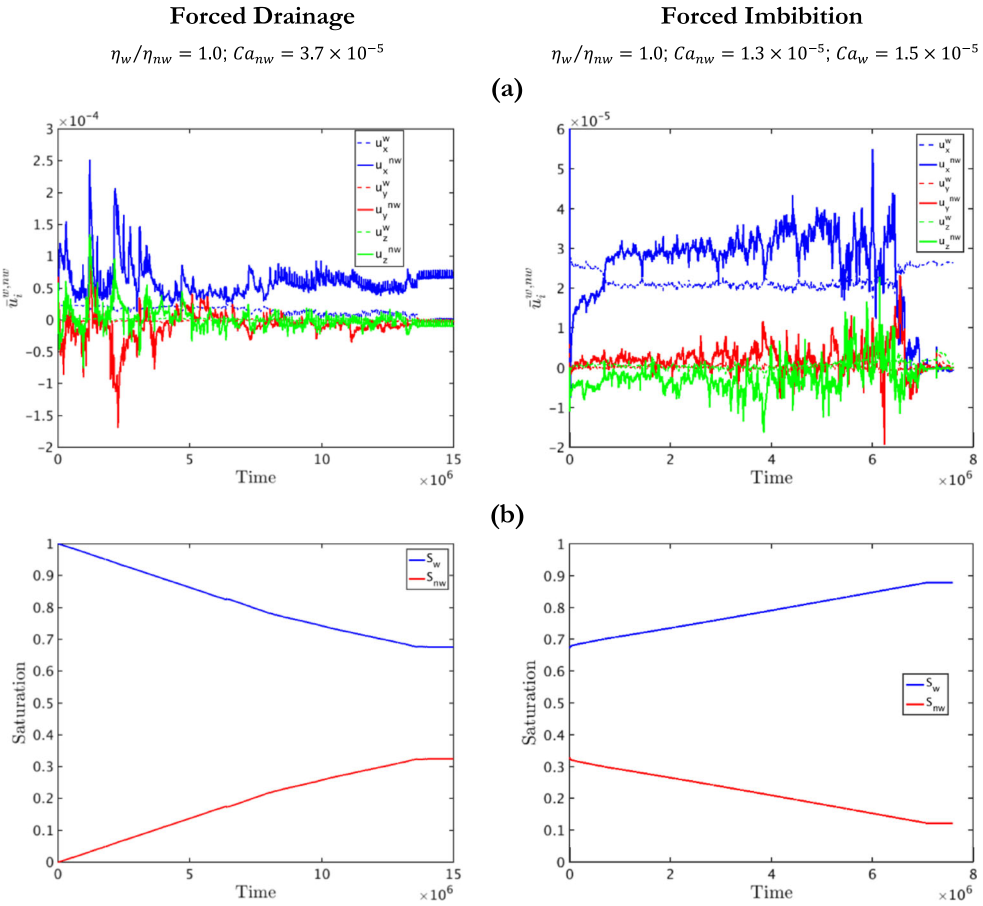

Fig. 26 Plots for forced-drainage and forced-imbibition processes simulated with the Castlegate sandstone image (w: wetting phase; nw: non-wetting phase). Forced imbibition starts from the end-point of the forced drainage. **a** Average (over the pore space) velocity components for the wetting and non-wetting phases as a function of time. **b** Average (over the pore space) saturation for the wetting and non-wetting phases as a function of time

jumps are noticeable in these plots, but their periodicity is less distinct compared to the more spherically grained Ketton limestone. A comparison of the frames in Fig. 26a to the frames in Fig. 14 indicates that, for the Castlegate sandstone, Haines jumps are detectable, but their periodicity is significantly more complex compared to the more granular Ketton limestone. Average (over the pore space) saturation for the wetting and non-wetting phases as a function of time for forced-drainage and forced-imbibition processes is illustrated in Fig. 26b. Post-drainage and post-imbibition non-wetting-phase fluid configurations are visualized for the Castlegate sandstone image in Fig. 27.

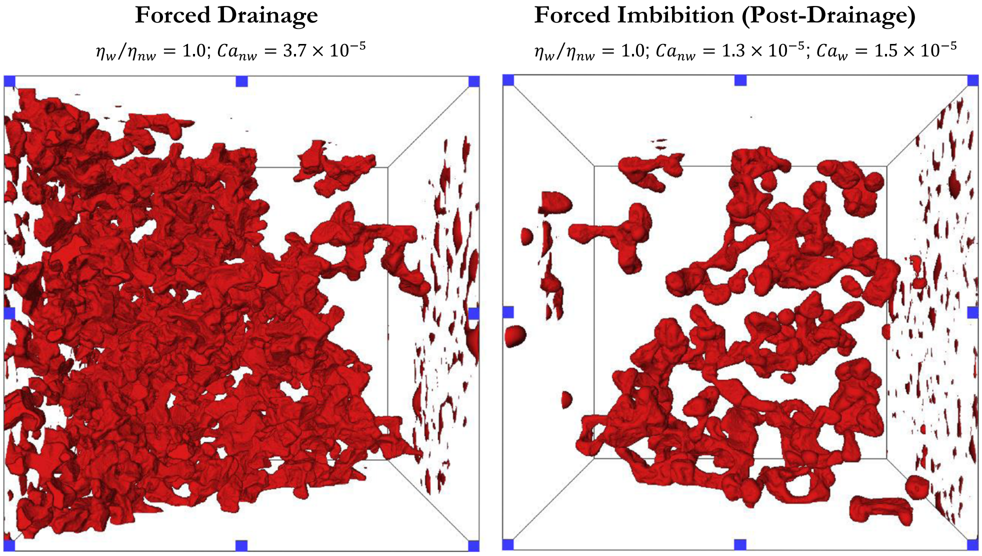

Fig. 27 Post-drainage and post-imbibition non-wetting phase fluid configurations are visualized for the Castlegate sandstone image. Inlet and outlet buffers are excluded in the visualization

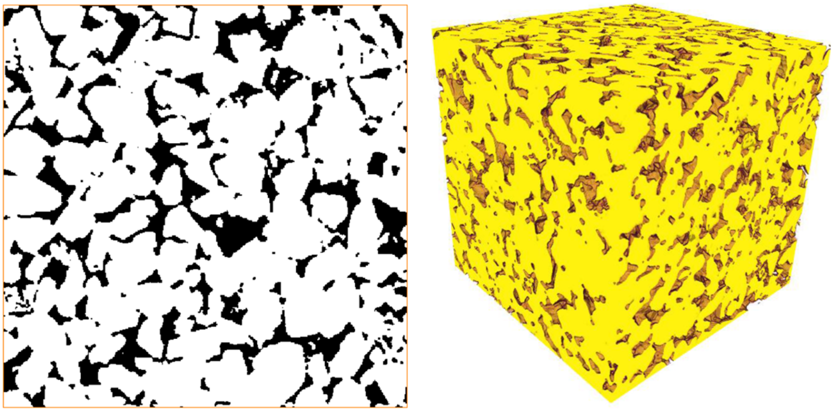

Fig. 28 Geometry used for the eLBM simulations of the Berea sandstone. The simulation system size is 400 × 400 × 400 lattice units (l.u.) at a resolution of 5.4 µm per l.u., which corresponds to a physical system size of (2.16 × 2.16 × 2.16 mm^3) and a porosity of 0.196. A small reservoir (16 l.u.) is added at the inlet/outlet of the domain for two-phase flow simulations

3.4 Capillary desaturation

The process where the non-wetting phase is mobilized by increasing the balance of (mobilizing) viscous forces over the (trapping) capillary forces is termed as capillary desaturation [48]. Capillary desaturation is the basis of many IOR and EOR processes such as water and surfactant flooding [62]. Since they are time consuming to measure experimentally [50], there is increasing interest to determine capillary desaturation curves using pore-scale flow-simulation approaches [58, 77, 98]. The concept is based on a visco-capillary balance over non-wetting-phase clusters (10, 48, and references therein).

In the following, the eLBM's capability for computing capillary desaturation curves is demonstrated. For the validation of eLBM using data reported in the literature [62], simulations are performed on a digitized water-wet Berea sandstone sample with a porosity of 0.20 and an absolute permeability of 1653 mD (Fig. 28). A similar study was reported in Koroteev et al. [58] using a proprietary simulator. The porosity and permeability of the Berea sandstone sample used in that work were 0.23 mD and 1150 mD, respectively. Neither of these references explicitly report the densities and viscosities of the fluids involved and the interfacial tension at their interface. We used the following values for water and decane (oil) at 25°C: $\rho_{water} = 1000$ kg/m^3 and $\rho_{oil} = 730$ kg/m^3; $\eta_{water} = 1.0$ cp and $\eta_{oil} = 0.89$ cp; $\sigma = 51.8 \times 10^{-3}$ N/m. Since we assume binary density–matched fluids in eLBM, only the viscosity ratio and interfacial tension are relevant for the numerical simulations. Following the experimental workflow in Lake [62], the model was initially filled with 100% of the non-wetting oil. Subsequently, it was flooded by the wetting phase (water) as shown in Fig. 29. Water injection was modeled at different capillary numbers (Ca) and continued until residual oil saturation was established. We control Ca

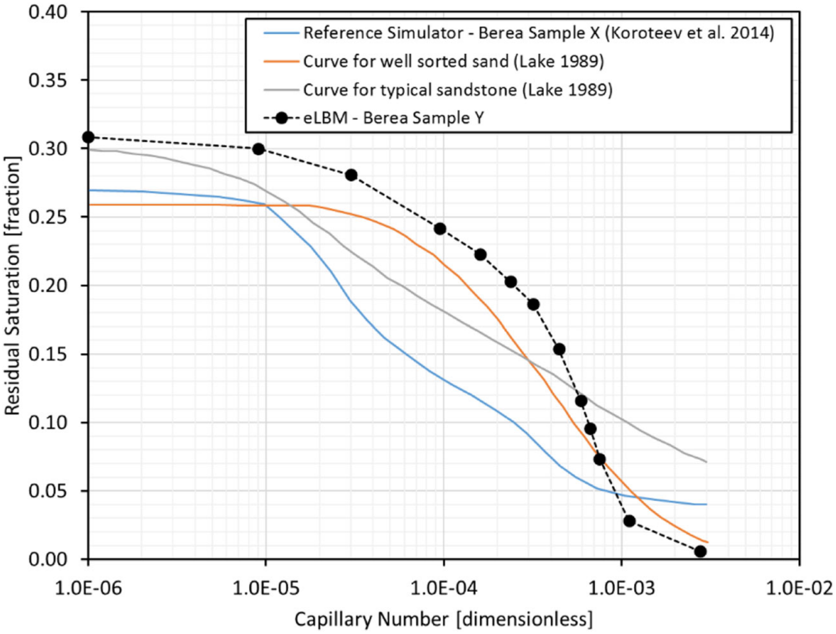

Fig. 29 Experimental and numerically simulated capillary desaturation curves for sandstone rocks. Digital rock flow simulations are performed on the Berea sandstone micro-CT images

by controlling the displacement velocity in our numerical simulations. The capillary desaturation curve calculated by eLBM (Fig. 29) is in a reasonable agreement with experimental data [62] and proprietary simulator predictions [58] for the investigated Ca values. It is important to note that different samples were used in the reported studies, which explains the differences in the residual oil observations.

4 Summary and conclusions

We describe the mathematics, validation, and applications of a novel Helmholtz free-energy—minimizing phase-field model solved within the framework of the LBM for efficiently simulating two-phase pore-scale flow directly on large 3D images of real rocks obtained from micro-computed tomography (micro-CT) scanning. The code implementation of the technique, eLBM, is performed in the CUDA programming language to take maximum advantage of accelerated computing by use of multinode GPGPUs.

eLBM's momentum-balance solver is based on the MRT model. The Boltzmann equation is discretized in space, velocity (momentum), and time coordinates using a D3Q19 scheme, which provides the best compromise between accuracy and computational efficiency. The benefits of the MRT model over the conventional single-relaxation-time BGK model are (I) enhanced numerical stability, (II) independent bulk and shear viscosities, and (III) viscosity-independent, nonslip boundary conditions. The drawback of the MRT model is that it is slightly more computationally demanding compared to the BGK model. This minor challenge is easily overcome through a GPGPU implementation of the MRT model for eLBM. eLBM is, to our knowledge, the first industrial grade–distributed parallel implementation of an energy-based LBM taking advantage of multiple GPGPU nodes. The Cahn-Hilliard equation that governs the order-parameter distribution is fully integrated into the LBM framework that accelerates the pore-scale simulation on real systems significantly.

Our novel contributions are (1) integrating all computational and high-performance computing components together into a unified implementation and (2) providing definitive quantitative validation results with eLBM in terms of robustness and accuracy for a variety of flow domains including a plethora of real rock images. We successfully validate and apply the eLBM on several transient two-phase flow problems of gradually increasing complexity. Successfully simulated validation problems include the following: (1) modeling of snap-off phenomena in constricted capillary tubes while honoring the Roof criterion; (2) capturing the correct time scales and velocity, saturation, and pressure profiles of Haines jumps on a micromodel, a Ketton limestone image, a Fontainebleau sandstone image, and a Castlegate sandstone image; and (3) capillary desaturation simulations on a Berea sandstone image including a comparison of numerically computed residual non-wetting-phase saturations to data reported in the literature.

Extensive physical validation tests and applications on large 3D rock images demonstrate the reliability, robustness, and efficacy of the eLBM as a direct visco-capillary pore-scale two-phase flow simulator for digital rock physics workflows. Future work will focus on enhancing the distributed parallel performance of eLBM through code optimization.

References

1. Alpak, F.O., Berg, S., Zacharoudiou, I.: Prediction of fluid topology and relative permeability in imbibition in sandstone rock by direct numerical simulation. Adv. Water Resour. **122**, 49–59 (2018)
2. Alpak, F.O., Gray, F., Saxena, N., Dietderich, J., Hofmann, R., Berg, S.: A distributed parallel multiple-relaxation-time lattice Boltzmann method on general-purpose graphics processing units for the rapid and scalable computation of absolute permeability from high-resolution 3D micro-CT images. Comput. Geosci. **22**, 815–832 (2018)
3. Alpak, F.O., Riviere, B., Frank, F.: A phase-field method for the direct simulation of two-phase flows in pore-scale media using a non-equilibrium wetting boundary condition. Comput. Geosci. **20**, 881–908 (2016)
4. Alpak, F.O., Samardžić, A., Frank, F.: A distributed parallel direct simulator for pore-scale two-phase flow on digital rock images using a finite difference implementation of the phase-field method. J. Pet. Sci. Eng. **166**, 806–824 (2018)
5. Andrä, H., Combaret, N., Dvorkin, J., Glatt, E., Han, J., Kabel, M., Keehm, Y., Krzikalla, F., Lee, M., Madonna, C., Marsh, M., Mukerji, T., Saenger, E.H., Sain, R., Saxena, N., Ricker, S., Wiegmann, A., Zhan, X.: Digital rock physics benchmarks—part I: imaging and segmentation. Comput. Geosci. **50**, 25–32 (2013)
6. Andrä, H., Combaret, N., Dvorkin, J., Glatt, E., Han, J., Kabel, M., Keehm, Y., Krzikalla, F., Lee, M., Madonna, C., Marsh, M., Mukerji, T., Saenger, E.H., Sain, R., Saxena, N., Ricker, S., Wiegmann, A., Zhan, X.: Digital rock physics benchmarks—part II: computing effective properties. Comput. Geosci. **50**, 33–43 (2013)
7. Anderson, D.M., McFadden, G.B., Wheeler, A.A.: Diffuse-interface methods in fluid mechanics. Annu. Rev. Fluid Mech. **30**(1), 139–165 (1998)
8. Armstrong, R.T., Berg, S.: Interfacial velocities and capillary pressure gradients during Haines jumps. Phys. Rev. E **88**(4), 043010 (2013)
9. Armstrong, R.T., Berg, S., Dinariev, O., Evseev, N., Klemin, D., Koroteev, D., Safonov, S.: Modeling of pore-scale two-phase phenomena using density functional hydrodynamics. Transp. Porous Media **112**(3), 577–607 (2016)
10. Armstrong, R.T., Georgiadis, A., Ott, H., Klemin, D., Berg, S.: Critical capillary number: desaturation studied with fast X-ray computed microtomography. Geophys. Res. Lett. **41**, 1–6 (2014)
11. Armstrong, R.T., McClure, J.E., Berill, M.A., Rücker, M., Schlüter, S., Berg, S.: Beyond Darcy's law: the role of phase topology and Ganglion dynamics for two fluid flow. Phys. Rev. E. **94**, 043113 (2016)

12. Armstrong, R.T., McClure, J.E., Berill, M.A., Rücker, M., Schlüter, S., Berg, S.: Flow regimes during immiscible displacement. Petrophysics **58**(1), 10–18 (2017)
13. Badalassi, V.E., Ceniceros, H.D., Banerjee, S.: Computation of multiphase systems with phase field models. J. Comput. Phys. **190**, 371–397 (2003)
14. Benzi, R., Succi, S., Vergassola, M.: The lattice Boltzmann equation: theory and applications. Phys. Rep. **222**(3), 145–197 (1992)
15. Beresnev, I.A., Deng, W.: Theory of breakup of core fluids surrounded by a wetting annulus in sinusoidally constricted capillary channels. Phys. Fluids **22**, 012105 (2010)
16. Beresnev, I.A., Li, W., Vigil, R.D.: Condition for break-up of non-wetting fluids in sinusoidally constricted capillary channels. Transp. Porous Media **80**, 581–604 (2009)
17. Berg, S., Armstrong, R., Ott, H., Georgiadis, A., Klapp, S.A., Schwing, A., Neiteler, R., Brussee, N., Makurat, A., Leu, L., Enzmann, F., Schwarz, J.-O., Wolf, M., Khan, F., Kersten, M., Irvine, S., Stampanoni, M.: Multiphase flow in porous rock imaged under dynamic flow conditions with fast X-ray computed microtomography. Petrophysics **55**(4), 304–312 (2014)
18. Berg, S., Ott, H., Klapp, S.A., Schwing, A., Neiteler, R., Brussee, N., Makurat, A., Leu, L., Enzmann, F., Schwarz, J.-O., Kersten, M., Irvine, S., Stampanoni, M.: Real-time 3D imaging of Haines jumps in porous media flow. Proc. Natl. Acad. Sci. **110**(10), 3755–3759 (2013)
19. Berg, S., Rücker, M., Ott, H., Georgiadis, A., van der Linde, H., Enzmann, F., Kersten, M., Armstrong, R.T., de With, S., Becker, J., Wiegmann, A.: Connected pathway relative permeability from pore-scale imaging of imbibition. Adv. Water Resour. **90**, 24–35 (2016)
20. Bhatnagar, P.L., Gross, E.P., Krook, M.: A model for collision processes in gases. I. Small amplitude processes in charged and neutral one-component systems. Phys. Rev. **94**, 511–525 (1954)
21. Blunt, M.J., Bijeljic, B., Dong, H., Gharbi, O., Iglauer, S., Mostaghimi, P., Paluszny, A., Pentland, C.: Pore-scale imaging and modelling. Adv. Water Resour. **51**, 197–216 (2013)
22. Blunt, M.J., Jackson, M.D., Piri, M., Valvatne, P.H.: Detailed physics, predictive capabilities and macroscopic consequences for pore-network models of multiphase flow. Adv. Water Resour. **25**, 1069–1089 (2002)
23. Boek, E.S., Zacharoudiou, I., Gray, F., Shah, S.M., Crawshaw, J.P., Yang, J.: Multiphase-flow and reactive-transport validation studies at the pore scale by use of lattice Boltzmann computer simulations. SPE J. **22**(3), 940–949 (2017)
24. Briant, A.J., Yeomans, J.M.: Lattice Boltzmann simulations of contact line motion. II. Binary fluids. Phys. Rev. E **69**(3), 031603 (2004)
25. Briant, A.J., Wagner, A.J., Yeomans, J.M.: Lattice Boltzmann simulations of contact line motion. I. Liquid-gas systems. Phys. Rev. E **69**(3), 031602 (2004)
26. Cahn, J.: Critical-point wetting. J. Chem. Phys. **66**(8), 3367 (1977)
27. Cahn, J.W., Hilliard, J.E.: Free energy of a nonuniform system. I. Interfacial free energy. J. Chem. Phys. **28**(2), 258–267 (1958)
28. d'Humières, D., Ginzburg, I., Krafczyk, M., Lallemand, P., Luo, L.-S.: Multiple-relaxation-time lattice Boltzmann models in three dimensions. Philosophical Transactions of the Royal Society A – Mathematical. Phys. Eng. Sci. **360**(1792), 72 (2002)
29. de Gennes, P.G.: Wetting: statics and dynamics. Rev. Mod. Phys. **57**(3), 827–863 (1985)
30. Demianov, A., Dinariev, O., Evseev, N.V.: Density functional modelling in multiphase compositional hydrodynamics. Can. J. Chem. Eng. **89**, 206–226 (2011)
31. Demianov, A., Dinariev, O., Evseev, N.V.: Introduction to the density functional method in hydrodynamics. Moscow, Fizmatlit (2014)
32. DiCarlo, D.A., Cidoncha, J.I.G., Hickey, C.: Acoustic measurements of pore-scale displacements. Geophys. Res. Lett. **30**(17), 1901 (2003)
33. Dinariev, O., Evseev, N.: Multiphase flow modeling with density functional method. Comput. Geosci. **20**, 835–856 (2016)
34. Ding, H., Spelt, P.D.M., Shu, C.: Diffuse interface model for incompressible two-phase flows with large density ratios. J. Comput. Phys. **226**, 2078–2095 (2007)
35. Dong, B., Yan, Y., Li, W.: LBM simulation of viscous fingering phenomenon in immiscible displacement of two fluids in porous media. Transp. Porous Media **88**(2), 293–314 (2011)
36. Du, R., Shi, B., Chen, X.: Multi-relaxation-time lattice Boltzmann model for incompressible flow. Phys. Lett. A **359**(6), 564–572 (2006)
37. Ferrari, A., Lunati, I.: Inertial effects during irreversible meniscus reconfiguration in angular pores. Adv. Water Resour. **74**, 1–13 (2014)
38. Frank, F., Liu, C., Alpak, F.O., Berg, S., Riviere, B.: Direct numerical simulation of flow on pore-scale images using discontinuous Galerkin finite element method. SPE J. **23**(5), 1833–1850 (2018)
39. Frank, F., Liu, C., Scanziani, A., Alpak, F.O., Riviere, B.: An energy-based equilibrium contact angle boundary condition on jagged surfaces for phase-field methods. J. Colloid Interface Sci. **523**, 282–291 (2018)
40. Georgiadis, A., Berg, S., Makurat, A., Maitland, G., Ott, H.: Pore-scale micro-computed-tomography imaging: non-wetting phase cluster size distribution during drainage and imbibition. Phys. Rev. E **88**(3), 033002 (2013)
41. Ghassemi, A., Pak, A.: Numerical study of factors influencing relative permeabilities of two immiscible fluids flowing through porous media using lattice Boltzmann method. J. Pet. Sci. Eng. **77**(1), 135–145 (2011)
42. Glimm, J., Grove, J.W., Li, X.-L., Zhao, N.: Simple front tracking. In: Chen, G.-Q., DiBenedetto, E. (eds.) Contemporary mathematics. American Mathematical Society, 238, 133–149 (1999)
43. Guangwu, Y.: A Lagrangian lattice Boltzmann method for Euler equations. Acta Mech. Sinica **14**(2), 186–192 (1998)
44. Gunstensen, A.K., Rothman, D.H., Zaleski, S., Zanetti, G.: Lattice Boltzmann model of immiscible fluids. Phys. Rev. A **43**(8), 4320 (1991)
45. Haines, W.B.: Studies in the physical properties of soils, part V—the hysteresis effect in capillary properties, and the modes of water distribution associated therewith. J. Agric. Sci. **20**(1), 97–116 (1930)
46. He, X., Chen, S., Zhang, R.: A lattice Boltzmann scheme for incompressible multiphase flow and its application in simulation of Rayleigh–Taylor instability. J. Comput. Phys. **152**(2), 642–663 (1999)
47. Hecht, M., Harting, J.: Implementation of on-site velocity boundary conditions for D3Q19 lattice Boltzmann simulations. Journal of Statistical Mechanics: Theory and Experiment P01018 (2010)
48. Hilfer, R., Armstrong, R.T., Berg, S., Georgiadis, A., Ott, H.: Capillary saturation and desaturation. Phys. Rev. E. **92**, 063023 (2015)
49. Huang, H., Huang, J.-J., Lu, X.-Y.: Study of immiscible displacements in porous media using a color gradient-based multiphase lattice Boltzmann method. Comput. Fluids **93**, 164–172 (2014)
50. Humphry, K.J., Suijkerbuijk, B.M.J.M., van der Linde, H.A., Pieterse, S.G.J., Masalmeh, S.K.: Impact of wettability on residual oil saturation and capillary desaturation curves. International Symposium of the Society of Core Analysts held in Napa Valley,

California, USA, 16-19 September 2013. Paper SCA2013-025 (2013)

51. Inamuro, T., Ogata, T., Tajima, S., Konishi, N.: A lattice Boltzmann method for incompressible two-phase flows with large density differences. J. Comput. Phys. **198**(2), 628–644 (2004)
52. Jacqmin, D.: Calculation of two-phase Navier-Stokes flows using phase-field modeling. J. Comput. Phys. **155**, 96–127 (1999)
53. Jakobsen, H.A.: Chemical reactor modelling. Springer, Berlin (2008)
54. Joekar-Niasar, V., van Dijke, M.I.J., Hassanizadeh, S.M.: Pore-scale modeling of multiphase flow and transport: achievements and perspectives. Transp. Porous Media **94**, 461–464 (2012)
55. Kendon, V., Cates, M., Pagonabarraga, I., Desplat, J.-C., Bladon, P.: Inertial effects in three-dimensional spinodal decomposition of a symmetric binary fluid mixture: a lattice Boltzmann study. J. Fluid Mech. **440**, 147–203 (2001)
56. Kim, J.: A continuous surface tension force formulation for diffuse-interface models. J. Comput. Phys. **204**, 784–804 (2005)
57. Kim, J.: Phase-field models for multi-component fluid flows. Communications in Computational Physics **12**(3), 613–661 (2012)
58. Koroteev, D., Dinariev, O., Evseev, N., Klemin, D., Nadeev, A., Safonov, S., Gurpinar, O., Berg, S., van Kruijsdijk, C., Armstrong, R., Myers, M.T., Hathon, L., de Jong, H.: Direct hydrodynamic simulation of multiphase flow in porous rock. Petrophysics **55**(4), 294–303 (2014)
59. Koroteev, D., Dinariev, O., Evseev, N., Klemin, D., Safonov, S., Gurpinar, O., Berg, S., van Kruijswijk, C., Myers, M., Hathon, L., de Jong, H., Armstrong, R.T.: Application of digital rock technology for chemical EOR screening. Paper SPE 165258, EORC 2013 – SPE Enhanced Oil Recovery Conference 2-4 July 2013, Kuala Lumpur, Malaysia (2013)
60. Kupershtokh, A.L., Medvedev, D.A., Karpov, D.I.: On equations of state in a lattice Boltzmann method. Computers & Mathematics with Applications **58**(5), 965–974 (2009)
61. Ladd, A.J.C., Verberg, R.: Lattice-Boltzmann simulations of particle-fluid suspensions. J. Stat. Phys. **104**(5-6), 1191–1251 (2001)
62. Lake, L.W.: Enhanced oil recovery. Prentice-Hall Inc, Englewood Cliffs (1989)
63. Lallemand, P., Luo, L.-S.: Theory of the lattice Boltzmann method: dispersion, dissipation, isotropy, Galilean invariance, and stability. Phys. Rev. E. **61**(6), 6546–6562 (2000)
64. Li, J., Sultan, A.S.: Permeability computations of shale gas by the pore-scale Monte Carlo molecular simulations. Paper IPTC-18263-MS presented at the International Petroleum Technology Conference 6-9 December, Doha. Qatar (2015)
65. Li, Q., Wagner, A.J.: Symmetric free-energy-based multicomponent lattice Boltzmann method. Phys. Rev. E **76**, 036701 (2007)
66. Li, X., Wu, S., Song, J., Li, H., Wang, S.: Numerical simulation of pore-scale flow in chemical flooding process. Theor. Appl. Mech. Lett. **2**, 022008 (2011)
67. Liu, H., Valocchi, A.J., Kang, Q., Werth, C.: Pore-scale simulations of gas displacing liquid in a homogeneous pore network using the lattice Boltzmann method. Transp. Porous Media **99**(3), 555–580 (2013)
68. Liu, Z., Wu, H.: Pore-scale modeling of immiscible two-phase flow in complex porous media. Appl. Therm. Eng. **93**, 1394–1402 (2016)
69. Luo, L.-S.: Theory of the lattice Boltzmann method: lattice Boltzmann models for nonideal gases. Phys. Rev. E **62**, 4982–4996 (2000)
70. Meakin, P., Tartakovsky, A.M.: Modeling and simulation of pore-scale multiphase fluid flow and reactive transport in fractured and porous media. Rev. Geophys. **47**, RG3002 (2009)
71. Meldi, M., Vergnault, E., Sagaut, P.: An arbitrary Lagrangian–Eulerian approach for the simulation of immersed moving solids with lattice Boltzmann method. J. Comput. Phys. **235**, 182–198 (2013)
72. Moebius, F., Or, D.: Interfacial jumps and pressure bursts during fluid displacement in interacting irregular capillaries. J. Colloid Interface Sci. **377**(1), 406–415 (2012)
73. Mohanty, K.K., Davis, H.T., Scriven, L.E.: Physics of oil entrapment in water-wet rock. SPE Reserv. Eval. Eng. **2**(1), 113–128 (1987)
74. Morrow, N.R.: Physics and thermodynamics of capillary action in porous media. Ind. Eng. Chem. **62**(6), 32–56 (1970)
75. Niessner, J., Berg, S., Hassanizadeh, S.M.: Comparison of two-phase Darcy's law with a thermodynamically consistent approach. Transp. Porous Media **88**, 133–148 (2011)
76. Nourgaliev, R.R., Theofanous, T.G.: High fidelity interface tracking: unlimited anchored level set. J. Comput. Phys. **224**, 836–866 (2007)
77. Oughanem, R., Youssef, S., Bauer, D., Peysson, Y., Maire, E., Vizika, O.: A multi-scale investigation of pore structure impact on the mobilization of trapped oil by surfactant injection. Transp. Porous Media **109**, 673–692 (2015)
78. Pooley, C.M., Furtado, K.: Eliminating spurious velocities in the free-energy lattice Boltzmann method. Phys. Rev. E **77**(4), 046702 (2008)
79. Pooley, C.M., Kusumaatmaja, H., Yeomans, J.M.: Contact line dynamics in binary lattice Boltzmann simulations. Phys. Rev. E **78**, 056709 (2008)
80. Premnath, K.N., Abraham, J.: Three-dimensional multi-relaxation-time (MRT) lattice-Boltzmann models for multiphase flow. J. Comput. Phys. **22**(2), 539–559 (2007)
81. Prodanovic, M., Bryant, S.L.: A level set method for determining critical curvatures for drainage and imbibition. J. Colloid Interface Sci. **304**(2), 442–458 (2006)
82. Raeesi, B., Morrow, N.R., Mason, G.: Contact angle hysteresis at smooth and rough surfaces. Integration Geoconvention, Geoscience Engineering Partnership (2013)
83. Raeini, A.Q., Blunt, M.J., Bijeljic, B.: Modelling two-phase flow in porous media at the pore scale using the volume-of-fluid method. Comput. Phys. **231**, 5653–5668 (2012)
84. Roman, S., Abu-Al-Saud, M., Tokunaga, T., Wan, J., Kovscek, A., Tchelepi, H.A.: Measurements and simulation of liquid films during drainage displacements and snap-off in constricted capillary tubes. J. Colloid Interface Sci. **507**, 279–289 (2017)
85. Roof, J.R.: Snap-off of oil droplets in water-wet pores. SPE J. **10**(1), 85–90 (1970)
86. Sedghi, M., Piri, M., Goual, L.: Molecular dynamics of wetting layer formation and forced water invasion in angular nanopores with mixed wettability. J. Chem. Phys. **141**, 194703 (2014)
87. Seth, S., Morrow, N.R.: Efficiency of the conversion of work of drainage to surface energy for sandstone and carbonate. SPE Reserv. Eval. Eng. **10**(4), 338–347 (2007)
88. Shan, X., Chen, H.: Lattice Boltzmann model for simulating flows with multiple phases and components. Phys. Rev. E. **47**(3), 1815 (1993)
89. Silin, D., Patzek, T.: Pore space morphology analysis using maximal inscribed spheres. Physica A – Statistical Mechanics and its Applications **371**(2), 336–360 (2006)
90. Sivanesapillai, R., Falkner, N., Hartmaier, A., Steeb, H.: A CSF-SPH method for simulating drainage and imbibition at pore-scale resolution while tracking interfacial areas. Adv. Water Resour. **95**, 212–234 (2016)
91. Succi, S.: The lattice-Boltzmann equation. Oxford University Press, Oxford (2001)

92. Swift, M.R., Orlandini, E., Osborn, W.R., Yeomans, J.M.: Lattice Boltzmann simulations of liquid-gas and binary fluid systems. Phys. Rev. E **54**(5), 5041–5052 (1996)
93. Swift, M.R., Osborn, W.R., Yeomans, J.M.: Lattice Boltzmann simulation of non-ideal fluids. Phys. Rev. Lett. **75**(5), 830–833 (1995)
94. Tölke, J., Freudiger, S., Krafczyk, M.: An adaptive scheme using hierarchical grids for lattice Boltzmann multi-phase flow simulations. Comput. Fluids **35**(8), 820–830 (2006)
95. Yan, G., Dong, Y., Liu, Y.: An implicit Lagrangian lattice Boltzmann method for the compressible flows. Numer. Methods Fluids **51**(12), 1407–1418 (2006)
96. Yang, J.: Multi-scale simulation of multiphase multi-component flow in porous media using the lattice Boltzmann method. PhD dissertation Imperial College, London, UK (2013)
97. Yeomans, J.: Mesoscale simulations: lattice Boltzmann and particle algorithms. J. Phys. A Math. Theor. **369**(1), 159–184 (2006)
98. Youssef, S., Peysson, Y., Bauer, D., Vizitak, O.: Capillary desaturation curve prediction using 3D microtomography images. International Symposium of the Society of Core Analysts held in St. John's, Newfoundland and Labrador, Canada, 16-21 August 2015. Paper SCA2015-008 (2015)
99. Yuan, H.H., Swanson, B.F.: Resolving pore-space characteristics by rate-controlled porosimetry. Paper SPE-14892. SPE Form. Eval. **4**(1), 17–24 (1989)
100. Zacharoudiou, I., Boek, E.S.: Capillary filling and Haines jump dynamics using free energy lattice Boltzmann simulations. Adv. Water Resour. **92**, 43–56 (2016)
101. Zhang, J., Kwok, D.Y.: A mean-field free energy lattice Boltzmann model for multicomponent fluids. The European Physical Journal Special Topics **171**(1), 45–53 (2009)
102. Zheng, H., Shu, C., Chew, Y.-T.: A lattice Boltzmann model for multiphase flows with large density ratio. J. Comput. Phys. **218**(1), 353–371 (2006)

Publisher's note Springer Nature remains neutral with regard to jurisdictional claims in published maps and institutional affiliations.

Affiliations

F. O. Alpak[1,2] · I. Zacharoudiou[3] · S. Berg[4,5,6] · J. Dietderich[1] · N. Saxena[1]

I. Zacharoudiou
i.zacharoudiou@imperial.ac.uk

S. Berg
Steffen.Berg@shell.com

J. Dietderich
jedietderich@gmail.com

N. Saxena
Nishank.Saxena@shell.com

[1] Shell International Exploration and Production, Inc., 3333 Highway 6 S, Houston, TX 77082, USA

[2] Department of Computational and Applied Mathematics, Rice University, 6100 Main Street - MS 134, Houston, TX 77005, USA

[3] Qatar Carbonates and Carbon Storage Research Centre, Department of Chemical Engineering, Imperial College London, South Kensington Campus, London, SW7 2AZ, UK

[4] Shell Global Solutions International B.V., Badhuisweg 3, 1031 CM Amsterdam, The Netherlands

[5] Department of Earth Science and Engineering, Imperial College London, South Kensington Campus, London, SW7 2AZ, UK

[6] Department of Chemical Engineering, Imperial College London, South Kensington Campus, London, SW7 2AZ, UK